Splitting-Based Structure Preserving Discretizations for Magnetohydrodynamics

RALF HIPTMAIR & CECILIA PAGLIANTINI

Splitting-Based Structure Preserving Discretizations for Magnetohydrodynamics

Ralf Hiptmair [1]
Cecilia Pagliantini [2]

[1] Seminar for Applied Mathematics, ETH Zürich, Zürich, Switzerland
E-mail address: ralf.hiptmair@sam.math.ethz.ch
[2] MCSS, École Polytechnique Fédérale de Lausanne, Lausanne, Switzerland
E-mail address: cecilia.pagliantini@epfl.ch.

Abstract. We start from the splitting of the equations of single-fluid magnetohydrodynamics (MHD) into a magnetic induction part and a fluid part. We design novel numerical methods for the MHD system based on the coupling of Galerkin schemes for the electromagnetic fields via finite element exterior calculus (FEEC) with finite volume methods for the conservation laws of fluid mechanics. Using a vector potential based formulation, the magnetic induction problem is viewed as an instance of a generalized transient advection problem of differential forms. For the latter, we rely on an Eulerian method of lines with explicit Runge–Kutta timestepping and on structure preserving spatial upwind discretizations of the Lie derivative in the spirit of finite element exterior calculus. The balance laws for the fluid constitute a system of conservation laws with the magnetic induction field as a space and time dependent coefficient, supplied at every time step by the structure preserving discretization of the magnetic induction problem. We describe finite volume schemes based on approximate Riemann solvers adapted to accommodate the electromagnetic contributions to the momentum and energy conservation. A set of benchmark tests for the two-dimensional planar ideal MHD equations provide numerical evidence that the resulting lowest order coupled scheme has excellent conservation properties, is first order accurate for smooth solutions, conservative and stable.

1. Introduction

The governing evolution equations of inviscid resistive MHD for spatially homogeneous and isotropic materials read (in non-dimensional form),

$$
\begin{cases}
\partial_t \rho + \operatorname{div}(\rho \mathbf{u}) = 0, & \text{(1.1a)} \\[4pt]
\partial_t(\rho \mathbf{u}) + \mathbf{div}\left(\rho \mathbf{u} \otimes \mathbf{u} + p\mathbb{I}\right) = \mathbf{curl}\,\mathbf{B} \times \mathbf{B}, & \text{(1.1b)} \\[4pt]
\partial_t E^{\mathrm{hd}} + \operatorname{div}\left(\left(E^{\mathrm{hd}} + p\right)\mathbf{u}\right) = \mathbf{curl}\,\mathbf{B} \cdot \mathbf{E}, & \text{(1.1c)} \\[4pt]
\partial_t \mathbf{B} + \mathbf{curl}\,\mathbf{E} = \mathbf{0}, & \text{(1.1d)} \\[4pt]
\mathbf{curl}\,\mathbf{B} = \mathbf{J}, & \text{(1.1e)} \\[4pt]
\mathbf{J} = \varepsilon^{-1}(\mathbf{E} + \mathbf{u} \times \mathbf{B}). & \text{(1.1f)}
\end{cases}
$$

Here ρ is the fluid density, p the pressure, $\mathbf{u}$ the fluid velocity and E^{hd} the hydrodynamic energy, all scaled appropriately. The electromagnetic quantities are the magnetic induction field $\mathbf{B}$, the current $\mathbf{J}$ and the electric field $\mathbf{E}$. The quantity ε is a symmetric positive semi-definite tensor representing the ratio of the electric resistivity and the magnetic permeability. The total energy E is expressed through

the equation of state $E = E^{\mathrm{hd}} + 1/2\|\mathbf{B}\|_{L^2}^2 = p/(\gamma - 1) + 1/2\rho\|\mathbf{u}\|_{L^2}^2 + 1/2\|\mathbf{B}\|_{L^2}^2$, where γ is the gas constant.

Initial conditions ensure $\mathrm{div}\mathbf{B} = 0$ which permits us to introduce a vector potential $\mathbf{A}$ such that, enforcing its uniqueness through the so-called temporal gauge,

$$\mathbf{curl}\,\mathbf{A} = \mathbf{B} \quad , \quad \mathbf{E} = -\partial_t\mathbf{A} - \mathrm{grad}(\mathbf{u} \cdot \mathbf{A}).$$

After the elimination of $\mathbf{E}$, $\mathbf{B}$, and $\mathbf{J}$ equations (1.1d)-(1.1f) can be replaced with

$$\partial_t\mathbf{A} + \varepsilon\,\mathbf{curl}\,\mathbf{curl}\,\mathbf{A} + \mathbf{curl}\,\mathbf{A} \times \mathbf{u} + \mathrm{grad}(\mathbf{u} \cdot \mathbf{A}) = \mathbf{0}. \tag{1.2}$$

Numerical methods for MHD are usually based on recasting (1.1) as a nonlinear system of conservation laws, keeping $\mathbf{B}$ as electromagnetic "conserved variable". This system is subsequently tackled by means of schemes of finite volume (FV) or discontinuous Galerkin (DG) type employing suitable numerical fluxes. Apart from shock resolution, a big challenge for these approaches is the preservation of the divergence constraint $\mathrm{div}\mathbf{B} = 0$, whose violation will inevitably trigger non-physical behavior of numerical solutions [40].

We pursue a radically different approach comprising the following key elements:

(1) Following the strategy introduced in [28], we split (1.1) into the so-called *extended Euler* equations (1.1a)-(1.1c), a system of conservation laws for the fluid quantities, and Maxwell's equations in the magneto-quasistatic approximation for the electromagnetic fields. Here we rely on the advection-diffusion equation (1.2) for the magnetic vector potential. Both parts are discretized in space independently, with the magnetic induction $\mathbf{B} = \mathbf{curl}\,\mathbf{A}$ and velocity $\mathbf{u}$ treated as parameters.

(2) We use the magnetic vector potential $\mathbf{A}$ as a primary electromagnetic quantity so that $\mathrm{div}\mathbf{B} = 0$ is exactly satisfied for $\mathbf{B} = \mathbf{curl}\,\mathbf{A}$.

(3) The discretization of the magnetic advection-diffusion equation takes the cue from Finite Element Exterior Calculus [3, 4, 25] using a Galerkin approach and discrete differential forms, here incarnated through families of $\mathrm{H}(\mathbf{curl}, \Omega)$-conforming finite elements.

(4) A mesh-based Eulerian discretization of (1.2) entails stabilization in the case of dominant transport $\varepsilon \approx 0$. We rely on upwinding introduced, in Section 2, through extrusion contraction discretization of the Lie derivative of discrete differential forms.

(5) For the spatial discretization of the extended Euler system (1.1a)-(1.1c) we employ, in Section 3, one of the many established FV or DG schemes, suitably adjusted in order to accommodate the presence of the magnetic induction $\mathbf{B} = \mathbf{curl}\,\mathbf{A}$. The latter will enter the underlying numerical fluxes as parameter.

Owing to Items 1, 3, 5, we have dubbed our new method the FV-FEEC scheme for MHD, see Section 3.2. We believe that Item 3 is a truly novel aspect. To the best of our knowledge, edge and face elements have only been employed in the development of mixed finite element discretizations of incompressible resistive MHD with partial Lie derivative in [36], and more recently in [26]. However, robustness of the aforementioned schemes with respect to large magnetic Reynolds number is still an issue as they rely on standard discretizations of the transport operator.

Remark 1.1. In the framework of our FEEC-based discretization the exterior derivative commutes with both the transport operator (Lie derivative, see Proposition 2.6) and stable projections onto the finite element spaces. Thus, $\mathbf{B} = \mathbf{curl}\,\mathbf{A}$ can be recovered without loss of accuracy, and, for the pure transport problem, a $\mathbf{B}$-based scheme would produce exactly the same results.

In this work we focus on the case $\varepsilon = 0$ known as *ideal MHD*. We consider this the most challenging situation, because magnetic diffusion as present for $\varepsilon > 0$ will smoothen shocks and enhance stability of spatial discretizations.

Beyond ideal MHD, extending the FV-FEEC approach to resistive MHD (1.1) is straightforward: We need only augment the discrete magnetic transport equation (1.2) with a conventional conforming Galerkin discretization of the diffusion operator $\varepsilon\mathbf{curl}\,\mathbf{curl}\,\mathbf{A}$ [25, Section 5]. As easy is the seamless coupling of the resistive MHD model (1.1) with a standard eddy current model in order to cover situations outlined in Figure 1.1. If the plasma is confined to a bounded region in space, zero outflow conditions can be imposed for the fluid model at its boundary, whereas the FEEC discretization of the $\mathbf{A}$-based formulation of the magneto-quasistatic equations can be used everywhere. It will ensure tangential continuity of both the magnetic vector potential and of the magnetic field (in a weak sense) across the plasma boundary.

Magnetostatic domain ($\sigma = 0$): $\mathbf{curl}\,\mu^{-1}(\mathbf{x})\mathbf{curl}\,\mathbf{A} = \mathbf{0}$, $\mathrm{div}\,\mathbf{A} = 0$

Plasma domain:
$\mathbf{A}$-based resistive MHD model (1.1)-(1.2)

Metal electrodes ($\sigma > 0$)

Eddy current domain:
$\mathbf{curl}\,\mu^{-1}(\mathbf{x})\mathbf{curl}\,\mathbf{A} + \partial_t(\sigma(\mathbf{x})\mathbf{A}) = 0$

Plasma boundary: $\mathbf{u} \cdot \mathbf{n} = 0$

Truncation boundary: $\mu^{-1}(\mathbf{x})\mathbf{curl}\,\mathbf{A} = \mathbf{g}$, $\mathbf{A} \cdot \mathbf{n} = 0$
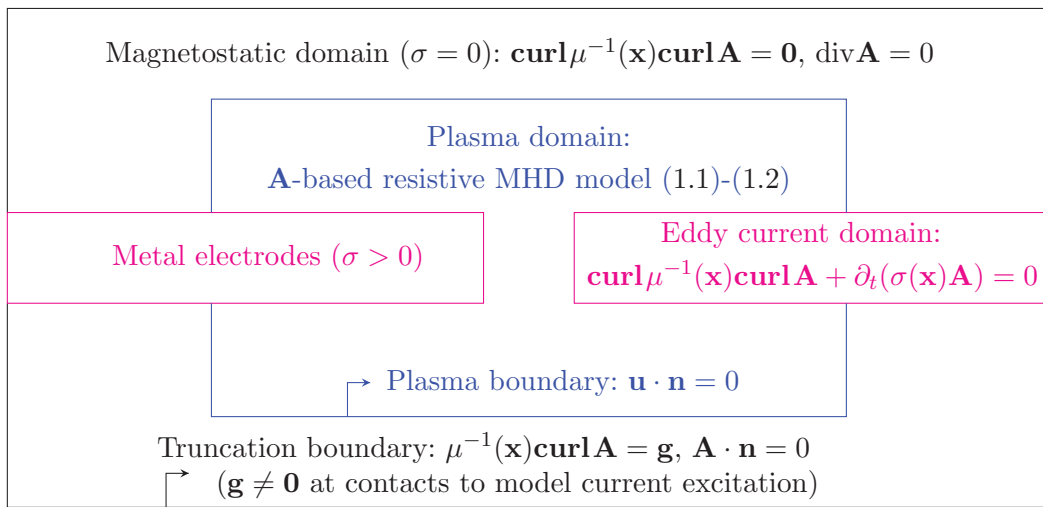($\mathbf{g} \neq \mathbf{0}$ at contacts to model current excitation)

FIGURE 1.1. High-current circuit breaker set-up: resistive MHD inside an air chamber has to be coupled with an eddy current model outside. The symmetric positive semidefinite tensors $\sigma = \sigma(\mathbf{x})$ and $\mu = \mu(\mathbf{x})$ represent the spatially varying fluid electric conductivity and magnetic permeability, respectively.

The ease with which our FV-FEEC scheme can accommodate non-coinciding fluid and electromagnetic domains contrasts sharply with the difficulties faced by conventional FV techniques in such situations. We regard this as a key advantage of our new method. However, we emphasize that comparison of FV-FEEC schemes with more conventional methods is beyond the scope of this article. In Section 4 we report the behavior of our new method for several initial value problems for (1.1) (with $\varepsilon = 0$) which serve as benchmark problems in the computational MHD literature. This makes it possible for the reader to compare the quality of solutions. Additional comments can be found in the concluding Section 5.

2. **Extrusion Contraction Discretization for the Generalized Pure Advection Evolution Problem**

The linear eddy current problem underlying the resistive MHD model, in the presence of a conducting fluid moving with velocity $\mathbf{u} = \mathbf{u}(\mathbf{x}, t)$, boils down to the evolution PDE (1.2) for the vector potential $\mathbf{A}$. Problem (1.2) and the well-known scalar advection-diffusion problem belong to a single family of

second order evolution problems, the so-called *generalized advection-diffusion* problem. In the spirit of FEEC, for a unified statement we rely on the language of exterior calculus: for differential k-forms in $\Omega \times I$, with Ω bounded Lipschitz domain in $\mathbb{R}^n$ and $I := [0, T]$, the strong form of the generalized advection-diffusion problem reads

$$\star \partial_t \omega(t) + (-1)^{k+1} \mathsf{d}^{n-k-1} \varepsilon \star \mathsf{d}^k \omega(t) + \star \mathrm{L}_{\mathbf{u}} \omega(t) = f(t), \qquad \text{in } \Omega \times I, \tag{2.1a}$$

$$\mathrm{tr}\, \omega(t) = g(t), \qquad \text{on } (\Gamma_{\mathrm{in}} \cup \Gamma_0) \times I, \tag{2.1b}$$

$$\mathrm{tr}(\mathsf{i}_{\mathbf{n}} \omega(t)) = s(t), \qquad \text{on } \Gamma_{\mathrm{in}} \times I, \tag{2.1c}$$

$$\omega(0) = \omega_0, \qquad \text{in } \Omega, \tag{2.1d}$$

where $\omega(t) \in \Lambda^k(\Omega)$ is a time-dependent differential k-form on Ω and $\mathbf{u} : \overline{\Omega} \times I \to \mathbb{R}^n$ is a *given* velocity field assumed to be *Lipschitz continuous*. The diffusion coefficient $\varepsilon : \Omega \to \mathbb{R}$ is a non-negative and bounded function, and the boundary conditions are imposed at the inflow boundary $\Gamma_{\mathrm{in}} := \{\mathbf{x} \in \partial\Omega : \mathbf{u} \cdot \mathbf{n}(\mathbf{x}) < 0\}$, and at $\Gamma_0 := \{\mathbf{x} \in \partial\Omega : \varepsilon > 0\}$. The forcing term and boundary data are $f(t) \in L^2\,\Lambda^{n-k}(\Omega)$, $g(t) \in L^2\Lambda^k(\Gamma_{\mathrm{in}} \cup \Gamma_0)$, and $s(t) \in L^2\Lambda^{k-1}(\Gamma_{\mathrm{in}})$. Using the standard notation of exterior calculus, see e.g. [23, Section 1.1], $\star$ is the Hodge operator, d^k is the exterior derivative, $\mathsf{i}_{\mathbf{n}}$ is the contraction by the vector $\mathbf{n}$ normal to the boundary, and $\mathrm{L}_{\mathbf{u}}$ is the Lie derivative. We point out that (1.2) is an instance of (2.1a) for $k = 1$ in three dimensions written in terms of so-called *Euclidean vector proxies*, see [22, Section 2].

It is well known that for the scalar advection-diffusion equation standard Galerkin discretizations with Lagrangian finite elements break down in the singular perturbation limit of vanishing diffusion. The observed onset of spurious oscillations reflects the weakly coercive nature of the problem in the energy norm. A plethora of stabilization mechanisms have been devised to curb unphysical oscillations while avoiding an excessive smearing of the solution [35].

In this work, we explore a class of finite element conforming discretizations of the transport operator built on the duality between the contraction operator and the extrusion of manifolds. The terminology extrusion contraction upwind schemes was introduced in [21] where the authors proposed a numerical approximation of the advection-diffusion problem, with focus on the scalar case, inspired by the discretization of the contraction introduced in [8]. A finite-volume-like discretization of the transient pure advection problem for 1-forms based on a similar technique was later suggested in [31].

With the ideal MHD problem in mind, we focus on the transient generalized *pure advection* problem ($\varepsilon = 0$): numerical schemes proving robust in this case are also suitable for the generalized problem when augmented with a standard $H\Lambda^k(\Omega)$-conforming Galerkin discretization of the non-vanishing diffusion term. The generalized pure advection initial boundary value problem in the space-time domain $\Omega \times I$, in weak formulation reads: For $f \in C^0(I; L^2\Lambda^k(\Omega))$ and $\omega_0 \in W_{|t=0}$, find $\omega \in C^1(I; L^2\,\Lambda^k(\Omega)) \cap C^0(I; W)$ such that

$$(\partial_t \omega, \eta)_\Omega + (\alpha\omega, \eta)_\Omega + (\mathrm{L}_{\mathbf{u}} \omega, \eta)_\Omega = (f, \eta)_\Omega,$$
$$(\omega(0), \eta)_\Omega = (\omega_0, \eta)_\Omega, \tag{2.2}$$

for all $\eta \in L^2\,\Lambda^k(\Omega)$, where $(\cdot, \cdot)_\Omega$ denotes the $L^2\,\Lambda^k(\Omega)$ inner product $(\omega, \eta)_\Omega := \int_\Omega \omega \wedge \star\eta$, and the variational spaces V and W are defined as

$$V := \{\omega \in L^2\Lambda^k(\Omega) : \mathrm{L}_{\mathbf{u}}\omega \in L^2\Lambda^k(\Omega), \int_{\Gamma_{\mathrm{in}}} \mathrm{tr}\, \mathsf{i}_{-\mathbf{u}}(\omega \wedge \star\omega) < \infty\},$$

$$W_{|t} := \{\omega \in V : \mathrm{tr}\,\omega = g, \mathrm{tr}\,\mathsf{i}_{\mathbf{n}}\omega = s \text{ on } \Gamma_{\mathrm{in}}, g(t) \in L^2\Lambda^k(\Gamma_{\mathrm{in}}), s(t) \in L^2\Lambda^{k-1}(\Gamma_{\mathrm{in}})\}.$$

For velocity fields uniformly continuous in time and Lipschitz continuous in space, $\mathbf{u} \in C^0(I; W^{1,\infty}(\Omega))$, the following "coercivity" condition on the velocity: there exists a constant $\alpha_0 > 0$ such that

$$\int_\Omega (\alpha + \frac{1}{2}(\mathrm{L}_{\mathbf{u}(\cdot,t)} + \mathcal{L}_{\mathbf{u}(\cdot,t)}))\omega \wedge \star\omega \geq \alpha_0 \int_\Omega \omega \wedge \star\omega, \qquad \forall \omega \in L^2\Lambda^k(\Omega), \ \forall t \in I, \qquad (2.3)$$

with $\mathcal{L}_{\mathbf{u}} = -(-1)^{k(n-k)}\star\mathrm{L}_{\mathbf{u}}\star$, ensures that the variational problem (2.2) is well-posed. Expressions in vector proxies of the "coercivity" condition (2.3) on the velocity field can be found in [33, Table 3.1]. However, MHD solutions feature shocks that give rise to *discontinuous velocities*. A well-posedness theory for velocity fields with less regularity is available only for scalar advection. We refer to [23, Section 1.2] for a more detailed discussion on the well-posedness of the generalized advection problem.

Following a method of lines strategy, a suitable spatial discretization of the time-independent advection operator can be coupled with an explicit Runge–Kutta scheme. Therefore, we first consider the stationary generalized advection boundary value problem for a k-form $\omega \in \Lambda^k(\Omega)$: Find $\omega \in V$ such that

$$\alpha\omega + \mathrm{L}_{\mathbf{u}}\omega = f, \quad \text{in } \Omega, \quad \mathrm{tr}\,\omega = g\,, \ \mathrm{tr}\,i_{\mathbf{n}}\omega = s, \quad \text{on } \Gamma_{\mathrm{in}}, \qquad (2.4)$$

with $f \in L^2\Lambda^k(\Omega)$, $g \in L^2\Lambda^k(\Gamma_{\mathrm{in}})$, $s \in L^2\Lambda^{k-1}(\Gamma_{\mathrm{in}})$. We aim at finding a stable numerical discretization of the advection operator, the Lie derivative $\mathrm{L}_{\mathbf{u}}$, based on polynomial $H\Lambda^k(\Omega)$-conforming discrete differential forms.

In the following, let $\{\mathcal{T}_h\}_{h>0}$ be a family of cellular decompositions of the domain Ω such that every $\mathcal{T}_h$ is either a finite element simplicial mesh in the sense of Ciarlet [10, Section 3.1], or it is a tensor product mesh. Let $\Delta_j(\mathcal{T}_h)$ denote the set of all j-faces of $\mathcal{T}_h$ with the convention $\Delta_n(\mathcal{T}_h) = \mathcal{T}_h$. Furthermore, let $\Lambda^k_h(\mathcal{T}_h)$, $0 \leq k \leq n$, be an $H\Lambda^k(\Omega)$-conforming space of piecewise polynomial *discrete differential forms*, see e.g. [3, Section 5]. Let $\Lambda^k_{h,r}(\mathcal{T}_h)$, $0 \leq k \leq n$, be the $H\Lambda^k(\Omega)$-conforming space of piecewise polynomial discrete differential k-forms of degree at most $r \geq 1$, namely

$$\Lambda^k_{h,r}(\mathcal{T}_h) := \{\omega_h \in H\Lambda^k(\Omega) : \omega_{h|T} \in \zeta^k_r(T), \ T \in \mathcal{T}_h\}, \qquad (2.5)$$

where the local shape functions are $\zeta^k_r(T) = \mathcal{P}_r\Lambda^k(T)$ or $\zeta^k_r(T) = \mathcal{P}^-_r\Lambda^k(T)$ on simplicial meshes [24, 3], and $\zeta^k_r(T) = \mathcal{Q}^-_r\Lambda^k(T)$ [2] or $\zeta^k_r(T) = \mathcal{S}_r\Lambda^k(T)$ [1] on Cartesian meshes.

Let $0 \leq k \leq n$ and $r \geq 1$. On a n-cell $T \in \mathcal{T}_h$, the degrees of freedom (DOF) of $\zeta^k_r(T)$ are defined on every j-cell $f_j \in \Delta_j(T)$, with $k \leq j \leq M^{r,k}_{\min}$, as

$$\omega \in \zeta^k_r(T) \longmapsto W^\ell_{f_j}(\omega) := \int_{f_j} \mathrm{tr}\,\omega \wedge \eta^\ell_j \qquad \forall \ell = 1, \ldots, N_j, \qquad (2.6)$$

where $\{\eta^\ell_j\}^{N_j}_{\ell=1}$ is a basis of $\overline{\zeta}^k_{r,j}(T)$ defined as

$$\overline{\zeta}^k_{r,j}(T) := \begin{cases} \mathcal{P}^-_{r-j+k}\Lambda^{j-k}(f_j), & \text{if } \zeta^k_r(T) = \mathcal{P}_r\Lambda^k(T), \\ \mathcal{P}_{r-j+k-1}\Lambda^{j-k}(f_j), & \text{if } \zeta^k_r(T) = \mathcal{P}^-_r\Lambda^k(T), \\ \mathcal{P}_{r-2(j-k)}\Lambda^{j-k}(f_j), & \text{if } \zeta^k_r(T) = \mathcal{S}_r\Lambda^k(T), \\ \mathcal{Q}_{r-1}\Lambda^{j-k}(f_j), & \text{if } \zeta^k_r(T) = \mathcal{Q}^-_r\Lambda^k(T). \end{cases} \qquad (2.7)$$

Degrees of freedom for discrete k-forms are associated with j-facets of the mesh, where

$$j \in \{k, \ldots, M^{r,k}_{\min}\}\,, \quad M^{r,k}_{\min} := \begin{cases} \min\{n, \lfloor r/2 \rfloor + k\} & \text{if } \Lambda^k_{h,r}(\mathcal{T}_h) = \mathcal{S}_r\Lambda^k(\mathcal{T}_h), \\ \min\{n, r+k-1\} & \text{otherwise.} \end{cases} \qquad (2.8)$$

Then DOF-based local projection operators onto polynomial spaces of differential forms $\mathcal{I}^k_{r,T} : \Lambda^k(T) \to \zeta^k_r(T)$, for every $T \in \mathcal{T}_h$, can be defined so that,

$$W^\ell_{f_j}(\mathcal{I}^k_{r,T}\,\omega) := \int_{f_j} \mathrm{tr}(\mathcal{I}^k_{r,T}\,\omega) \wedge \eta = \int_{f_j} \mathrm{tr}\,\omega \wedge \eta, \qquad \forall \eta \in \overline{\zeta}^k_{r,j}(T), \quad f_j \in \Delta_j(T), \quad k \leq j \leq M^{r,k}_{\min}.$$

When boundary conditions at the inflow boundary are prescribed as in (2.1b), (2.1c), we define

$$\Lambda_{0,r}^k\left(\mathcal{T}_h\right) := \{\omega_h \in \Lambda_{h,r}^k\left(\mathcal{T}_h\right): \ \mathrm{tr}\,\omega_h = g, \ \mathrm{tr}\,\mathsf{i_n}\omega_h = s \text{ on } \Gamma_{\mathrm{in}}\}, \tag{2.9}$$

and similarly we use $\Lambda_0^k\left(\mathcal{T}_h\right)$ to denote the spaces $\Lambda_h^k\left(\mathcal{T}_h\right)$ endowed with inflow boundary conditions.

2.1. **Contraction and Extrusion**

The Lie derivative is a coordinate-independent operator which measures the rate of change of a differential form along the flow of a vector field. It is the generalization to k-forms of the spatial part of the material derivative which measures the rate of change observed by a material particle moving with a fluid. Let $\mathcal{M}_n$ be a n-dimensional smooth manifold and let $\mathbf{u}$ be a smooth vector field on $\mathcal{M}_n$. By introducing the *flow* of the vector field $\mathbf{u}$ on the manifold $\mathcal{M}_n$, namely $\Phi : \mathbb{R} \times \mathcal{M}_n \to \mathcal{M}_n$ such that $\partial_t \Phi(t,x) = \mathbf{u}(\Phi(t,x),t)$ with $\Phi(0,x) = x$, the Lie derivative of a differential k-form $\omega \in \Lambda^k\left(\Omega\right)$ is

$$\mathrm{L_u}\omega = \left.\frac{d}{dt}\right|_{t=0}\Phi_t^*\omega.$$

A key identity is Cartan's "magic" formula for the Lie derivative of a k-form $\omega \in \Lambda^k\left(\Omega\right)$,

$$\mathrm{L_u}\omega = \mathsf{d}^{k-1}\mathsf{i_u}\omega + \mathsf{i_u}\mathsf{d}^k\omega. \tag{2.10}$$

Thus, defining a discrete Lie derivative boils down to finding discrete counterparts of the exterior derivative d^k and of the contraction operator $\mathsf{i_u}$. Calculation of the exterior derivative is a well-defined and purely local operation for discrete differential forms.

Greater difficulties are faced for the contraction $\mathsf{i_u}$. Recall that the contraction of alternating $(k+1)$-forms by a Lipschitz continuous vector field $\mathbf{u}$ is defined as the k-form such that $(\mathsf{i_u}\omega)(\mathbf{x})(v_1,\ldots,v_k) = \omega(\mathbf{x})(\mathbf{u}(\mathbf{x}),v_1,\ldots,v_k)$, for $\omega \in \mathrm{Alt}^{k+1}V$ and $(v_1,\ldots,v_k) \in V^k$, V being a real vector space and $\mathrm{Alt}^{k+1}V$ the space of alternating algebraic $(k+1)$-forms on V. *Pointwise* application of this formula yields a definition of the contraction operator for smooth differential forms. The correspondences between the contraction of differential forms and proxy fields is recalled in Table 2.1.

| $\omega \in \Lambda^k\left(\Omega\right)$	$k=0$	$k=1$	$k=2$	$k=3$
$\mathsf{i_u}\omega$	$-$	$\mathbf{u}\cdot\mathbf{w}$	$\mathbf{w}\times\mathbf{u}$	$w\mathbf{u}$

TABLE 2.1. Contraction of differential forms: exterior calculus notations and corresponding expressions for vector proxies $\mathbf{w}$, w in $\mathbb{R}^3$.

A pointwise definition of contraction is problematic for discrete differential forms, which fail to be totally continuous. In particular, for $\omega_h \in \Lambda_h^{k+1}\left(\mathcal{T}_h\right)$ we find $\mathsf{i_u}\omega_h \notin H\Lambda^k\left(\Omega\right)$ in general. In addition, DOF-based interpolation will not be possible, because the traces of $\mathsf{i_u}\omega_h$ onto facets are ambiguous.

2.2. **Upwind Discrete Contraction via Extrusion**

There is a less local way to understand contraction employing orbits of smooth manifolds under the flow, commonly called extrusion (see Figure 2.1).

Definition 2.1 (Extrusion). Let $\mathcal{M}_n$ be an n-dimensional smooth oriented manifold. Let $\mathcal{S}_j$ be a j-dimensional submanifold of $\mathcal{M}_n$, the extrusion $\mathsf{Ext_u}(\mathcal{S}_j,t)$ of $\mathcal{S}_j$ by the smooth vector field $\mathbf{u}$, at time t, is the $(j+1)$-dimensional manifold formed by the union of the submanifolds obtained by sweeping $\mathcal{S}_j = \Phi(0,\mathcal{S}_j)$ along the flow of $\mathbf{u}$ to the submanifold $\Phi(t,\mathcal{S}_j)$. Specifically, $\mathsf{Ext_u}(\mathcal{S}_j,t) = \bigcup_{s\in[0,t]}\Phi(s,\mathcal{S}_j)$ with orientation given by $\partial\mathsf{Ext_u}(\mathcal{S}_j,t) = \Phi(t,\mathcal{S}_j) - \Phi(0,\mathcal{S}_j) - \mathsf{Ext_u}(\partial\mathcal{S}_j,t)$.
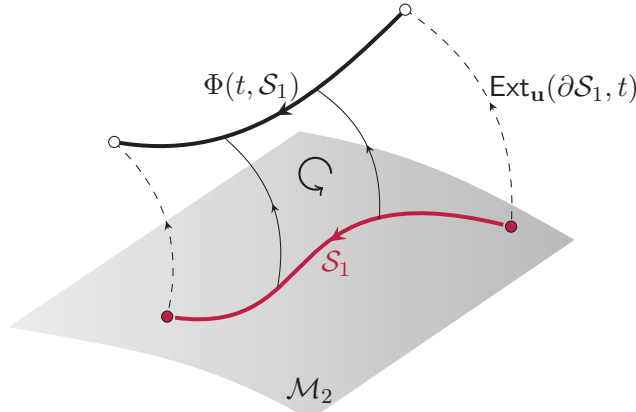
FIGURE 2.1. Sketch of the extrusion of an oriented path $\mathcal{S}_1$.

Then the contraction $i_{\mathbf{u}}\omega \in \Lambda^k(\mathcal{M}_n)$ of a smooth $(k+1)$-form $\omega \in \Lambda^{k+1}(\mathcal{M}_n)$ on a k-dimensional smooth oriented submanifold $\mathcal{M}_k$ can be defined as the instantaneous change of ω evaluated on the extrusion of $\mathcal{M}_k$ [8, Equation (14)], namely

$$\langle i_{\mathbf{u}}\omega, \mathcal{M}_k \rangle := \lim_{t \searrow 0} \frac{1}{t} \langle \omega, \mathsf{Ext}_{\mathbf{u}}(\mathcal{M}_k, t) \rangle, \tag{2.11}$$

where $\langle \cdot, \cdot \rangle$ denotes the chain-cochain duality pairing.

Since in FEEC we use integrals of forms as degrees of freedom, the concept of extrusion of a manifold by the flow of a vector field offers a natural way to define the integral of a contracted discrete differential form over such manifold. A discrete contraction and its combination with the coboundary operator pave the way to discretizations of the Lie derivative.

In greater detail, the duality formula (2.11) expresses the fact that the contraction of a smooth $(k+1)$-form over a k-dimensional manifold is equal to the instantaneous change of the form over the extrusion of the manifold. Equivalently for continuous ω, (2.11) can be rewritten with the k-dimensional submanifold $\mathcal{M}_k$ extruded *backward in time*:

$$\langle i_{\mathbf{u}}\omega, \mathcal{M}_k \rangle = -\lim_{t \searrow 0} \frac{1}{t} \langle \omega, \mathsf{Ext}_{\mathbf{u}}(\mathcal{M}_k, -t) \rangle, \qquad \forall \omega \in \Lambda^{k+1}(\mathcal{M}_n). \tag{2.12}$$

Owing to their lack of continuity, for discrete differential forms $\omega_h \in \Lambda_h^{k+1}(\mathcal{T}_h)$ the equivalence breaks down. In general,

$$\langle i_{\mathbf{u}}\omega_h, c_k \rangle = \lim_{t \searrow 0} \frac{1}{t} \int_{\mathsf{Ext}_{\mathbf{u}}(c_k, t)} \omega_h \quad \neq \quad -\lim_{t \searrow 0} \frac{1}{t} \int_{\mathsf{Ext}_{-\mathbf{u}}(c_k, t)} \omega_h = \langle -i_{-\mathbf{u}}\omega_h, c_k \rangle, \tag{2.13}$$

where $c_k \in \Delta_k(\mathcal{T}_h)$ is a k-face of $\mathcal{T}_h$.

This observation allows us to introduce *upwinding* by opting for the right-hand-side formula. For $\omega_h \in \Lambda^{k+1}(\mathcal{T}_h)$ in place of ω this yields well-defined point values for $i_{\mathbf{u}}\omega_h$ everywhere in Ω, even on facets of the mesh.

After deciding to use contraction based on upwind extrusion all facet-based degrees of freedom for $i_{\mathbf{u}}\omega_h$ are uniquely defined. Thus, a global contraction operator can be constructed through a (global) reconstruction, by interpolating the contraction of a discrete k-form into some space of $H\Lambda^{k-1}(\Omega)$-conforming discrete differential forms. Since we are interested in piecewise polynomial discretizations, we consider interpolation onto spaces of $H\Lambda^k(\Omega)$-conforming polynomial discrete differential forms $\Lambda_{h,p}^k(\mathcal{T}_h)$ of type (2.5), for some polynomial degree $p \geq 1$ which might differ from the polynomial degree of the approximation spaces.

As a preliminary step, in order to introduce an interpolation operator underlying contraction, we need to identify an "upwind direction" at the mesh facets.

Definition 2.2 (Upwind Element). Let $\mathcal{T}_h$ be a cellular complex on $\Omega \subset \mathbb{R}^n$. Consider a point $x \in \Omega$. The n-cell $T_x^{\mathsf{upw}} \in \mathcal{T}_h$ is said to *lie in the upwind direction* of x determined by the vector field $\mathbf{u}$, if the extrusion $\mathsf{Ext}_{-\mathbf{u}}(x,t)$ is (partly) contained in T_x^{upw} for t small enough. If $\mathsf{Ext}_{-\mathbf{u}}(x,t) \in f_j$ for some $f_j \in \Delta_j(\mathcal{T}_h)$, $1 \leq j < n$, then at least two n-cells are lying in the upwind direction of x. In this case, any $T \in \mathcal{T}_h$ such that $f_j \in \partial T$ can be selected as the upwind element at x, and the choice is arbitrary.

Note that in the limit of small t the upwind element at a given point $x \in \Omega$ is uniquely defined. A two-dimensional example of the elements lying in the upwind direction of points of an edge is shown in Figure 2.2.
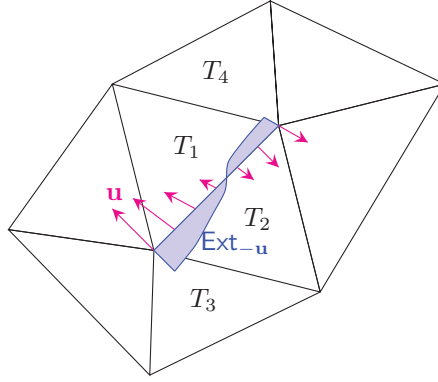

FIGURE 2.2. Two-dimensional example of the mesh elements lying in the upwind direction of points on an edge determined by the vector field $\mathbf{u}$.

Definition 2.3 (Upwind Interpolation of Contraction). Let $\mathcal{T}_h$ be a cellular complex on $\Omega \subset \mathbb{R}^n$. Let $\omega_h \in \Lambda_0^{k+1}(\mathcal{T}_h)$, $0 \leq k \leq n-1$, be a discrete differential $(k+1)$-form and let $\mathbf{u}$ be a smooth vector field. Consider a polynomial space of differential forms $\Lambda_{h,p}^k(\mathcal{T}_h) \subset H\Lambda^k(\Omega)$, $p \geq 1$, as in (2.5): let $\{\psi_j^\ell\}_{j,\ell}$ be a basis of $\Lambda_{h,p}^k(\mathcal{T}_h)$, and $M_{\min}^{p,k}$ the number of degrees of freedom (2.8) associated with the mesh faces. The upwind interpolation operator onto $\Lambda_{h,p}^k(\mathcal{T}_h)$ is defined as $\mathcal{I}_{\mathbf{u},p}^k : L^2\Lambda^k(\Omega) \to \Lambda_{h,p}^k(\mathcal{T}_h)$,

$$\mathcal{I}_{\mathbf{u},p}^k(\mathsf{i}_{\mathbf{u}}\omega_h) = \sum_{j=k}^{M_{\min}^{p,k}} \sum_{f_j \in \Delta_j(\mathcal{T}_h)} \sum_{\ell=1}^{N_j} W_{f_j}^\ell(\mathsf{i}_{\mathbf{u}}^{\mathsf{upw}}\omega_h)\, \psi_j^\ell,$$

where on a given j-facet $f_j \in \Delta_j(\mathcal{T}_h) \setminus \Gamma_{\mathrm{in}}$,
$$(\mathsf{i}_{\mathbf{u}}^{\mathsf{upw}}\omega_h)(x) := (\mathsf{i}_{\mathbf{u}}\omega_{h|_{T_x^{\mathsf{upw}}}})(x), \qquad \forall\, x \in f_j,$$

and T_x^{upw} is the element in the upwind direction of the point x determined by the vector field $\mathbf{u}$, as in Definition 2.2. The local degrees of freedom $W_{f_j}^\ell$ on every element $T \in \mathcal{T}_h$ are defined as,

$$W_{f_j}^\ell(\mathsf{i}_{\mathbf{u}}^{\mathsf{upw}}\omega_h) := \int_{f_j} \mathrm{tr}(\mathsf{i}_{\mathbf{u}}^{\mathsf{upw}}\omega_h) \wedge \eta_j^\ell, \qquad \forall f_j \in \Delta_j(T) \setminus \Gamma_{\mathrm{in}}, \tag{2.14}$$

$$W_{f_j}^\ell(\mathsf{i}_{\mathbf{u}}^{\mathsf{upw}}\omega_h) := \int_{f_j} \mathrm{tr}(\mathsf{i}_{\mathbf{u}}\omega_h) \wedge \eta_j^\ell, \qquad \forall f_j \in \Delta_j(T) \cap \Gamma_{\mathrm{in}}, \tag{2.15}$$

where $\{\eta_j^\ell\}_{\ell=1}^{N_j}$ is a basis of the local space $\overline{\zeta}_{r,j}^k(T)$ defined in (2.7).

Note that, owing to the regularity of discrete differential k-forms $\omega_h \in H\Lambda^k(\Omega)$, if the backward extrusion of a given point $x \in \Omega$ is contained in a j-facet $f_j \in \Delta_j(\mathcal{T}_h)$, $j < n$, then $\mathsf{i_u}\omega_{h|_T} = \mathsf{i_u}\omega_{h|_{T_x^{\mathrm{upw}}}}$ for all $T \in \mathcal{T}_h$ such that $f_j \in \partial T$. This justifies Definition 2.2. Moreover, $\mathcal{I}_{\mathbf{u},p}^k(\mathsf{i_u}\omega_h) = \mathsf{i_u}\omega_h$ if $\mathsf{i_u}\omega_h \in \Lambda_{h,p}^k(\mathcal{T}_h) \subset H\Lambda^k(\Omega)$. The degrees of freedom interior to the mesh elements are not affected by upwinding.

Remark 2.4 (Boundary conditions at the inflow boundary)**.** The evaluation of the interpolated contraction at the inflow boundary facets (2.15) relies on the fact that the trace of the form and the trace of its contraction, $\mathrm{tr}(\mathsf{i_n}\omega_h)$, at the inflow boundary of the domain are supplied by the boundary conditions (2.1b), (2.1c). One can decompose the velocity field $\mathbf{u}$ in its normal component $\mathbf{u_n} := (\mathbf{u}\cdot\mathbf{n})\mathbf{n}$ and its tangential component $\mathbf{u_t} := (\mathbf{n}\times\mathbf{u})\times\mathbf{n}$, such that

$$\mathsf{i_u}\omega_h = \mathsf{i_{u_n}}\omega_h + \mathsf{i_{u_t}}\omega_h = (\mathbf{u}\cdot\mathbf{n})\mathsf{i_n}\omega_h + \mathsf{i_{u_t}}\omega_h, \qquad \forall\,\omega_h \in \Lambda_h^k(\mathcal{T}_h),\,\forall k.$$

Note that the contraction by the tangential component of the velocity is available from the trace of ω_h (2.4). However, in the case of non-smooth boundaries, the contraction might not be uniquely defined at a given boundary j-cell, $j \le n-1$. One could average the contributions from the n-cells sharing the j-cell. For example, in two dimensions, at a boundary node $\mathbf{x} \in \Delta_0(\mathcal{T}_h) \cap \partial\Omega$ such that $\mathbf{x} \in \Delta_0(e_1) \cap \Delta_0(e_2)$ for some edges $e_1, e_2 \in \Delta_1(\mathcal{T}_h) \cap \partial\Omega$, one can approximate the contraction of a 1-form ω_h as

$$\mathsf{i_u}\omega_h \approx \frac{1}{2}((\mathbf{u}\cdot\mathbf{n}_1)\mathsf{i_{n_1}}\omega_h + \mathsf{i_{u_{t_1}}}\omega_h) + \frac{1}{2}((\mathbf{u}\cdot\mathbf{n}_2)\mathsf{i_{n_2}}\omega_h + \mathsf{i_{u_{t_2}}}\omega_h).$$

2.3. **Discrete Lie derivative**

Using the discretization of the contraction operator according to Definition 2.3, the *discrete* Lie derivative is defined as,

$$\boxed{\mathrm{L}_{\mathbf{u}}^h : \begin{cases} \Lambda_{0,r}^k(\mathcal{T}_h) \longrightarrow \Lambda_{h,p}^k(\mathcal{T}_h) \\ \qquad \omega_h \longmapsto \mathcal{I}_{\mathbf{u},p}^k(\mathsf{i_u}\mathsf{d}^k\omega_h) + \mathsf{d}^{k-1}\,\mathcal{I}_{\mathbf{u},p^-}^{k-1}(\mathsf{i_u}\omega_h), \end{cases}} \tag{2.16}$$

where $p^- \ge 1$ is such that $\mathsf{d}^{k-1}\Lambda_{h,p^-}^{k-1}(\mathcal{T}_h) \subset \Lambda_{h,p}^k(\mathcal{T}_h)$. The polynomial interpolation order p has to be chosen such that the consistency error does not destroy the accuracy order related to the finite element approximation. Moreover, in view of (2.12), the characterization (2.16) automatically incorporates an upwinding of the Lie derivative. Lastly, since $\mathbf{u}$ is Lipschitz continuous and the discrete differential forms are piecewise polynomials, the moments of the contracted forms on each j-cell of $\mathcal{T}_h$ are well-defined from within the n-cell in the upwind direction of the flow.

As a result of the discretization of the Lie derivative, the discrete advection problem, recast in weak form, reads: Find $\omega_h \in \Lambda_{0,r}^k(\mathcal{T}_h)$ such that

$$a_h(\omega_h, \eta_h) = (f, \eta_h)_\Omega, \qquad \forall\,\eta_h \in \Lambda_{h,r}^k(\mathcal{T}_h), \tag{2.17}$$

where the bilinear form $a_h(\cdot, \cdot)$ is defined, for all $\omega_h \in \Lambda_{0,r}^k(\mathcal{T}_h)$ and $\eta_h \in \Lambda_{h,r}^k(\mathcal{T}_h)$, as

$$a_h(\omega_h, \eta_h) := (\alpha\omega_h, \eta_h)_\Omega + \int_\Omega (\mathcal{I}_{\mathbf{u},p}^k(\mathsf{i_u}\mathsf{d}^k\omega_h) \wedge \star\eta_h + \mathsf{d}^{k-1}\,\mathcal{I}_{\mathbf{u},p^-}^{k-1}(\mathsf{i_u}\omega_h) \wedge \star\eta_h).$$

2.3.1. *Discrete Lie Derivative in Terms of Euclidean Vector Proxies*

We report the vector proxy representation of the discrete Lie derivative defined in (2.16), for $k = 0$ and $k = 1$ forms. These are the two cases of interest when dealing with the potential formulation of the MHD problem. Let V_h be finite element spaces of vector proxies associated with the spaces $\Lambda_{0,r}^k(\mathcal{T}_h)$

of polynomial differential k-forms of degree at most $r \geq 1$ on the three-dimensional cellular complex $\mathcal{T}_h$. Let $\mathcal{I}_{\mathbf{u},p}^k$, $0 \leq k \leq 2$, and $\mathcal{I}_{\mathbf{u},p^-}^k$, $1 \leq k \leq 3$, be upwind interpolation operators onto piecewise polynomial spaces of degree at most $p \geq 1$ and $p^- \geq 1$, respectively. Let $w_h \in V_h$ or $\mathbf{w}_h \in V_h$ be the vector proxy representation of the k-form $\omega_h \in \Lambda_{0,r}^k(\mathcal{T}_h)$ and let $M_{\min}^{p,k}$ be defined as in (2.8) for $n = 3$. The discrete Lie derivative (2.16) reads

$$k = 0: \qquad \mathrm{L}_{\mathbf{u}}^h w_h = \mathcal{I}_{\mathbf{u},p}^0(\mathsf{i}_\mathbf{u}\mathsf{d}^0 w_h) = \mathcal{I}_{\mathbf{u},p}^0(\mathbf{u} \cdot \operatorname{grad} w_h)$$

$$= \sum_{j=0}^{M_{\min}^{p,0}} \sum_{f_j \in \Delta_j(\mathcal{T}_h)} \sum_{\ell=1}^{N_j} W_{f_j}^\ell((\mathbf{u} \cdot \operatorname{grad} w_h)^{\mathsf{upw}})\lambda_j^\ell, \tag{2.18}$$

$$(\mathbf{u} \cdot \operatorname{grad} w_h)^{\mathsf{upw}}(x) := \mathbf{u}(x) \cdot (\operatorname{grad} w_h)_{|_{T_x^{\mathsf{upw}}}}(x), \qquad \forall\, x \in f_j \setminus \Gamma_{\mathrm{in}},$$

and boundary conditions are used whenever $x \in \Gamma_{\mathrm{in}}$. Here $\{\lambda_j^\ell\}_{j,\ell}$ is a basis of H^1-conforming polynomials of degree at most p.

Let $\{\phi_j^\ell\}_{j,\ell}$ be a basis of $\mathrm{H}(\mathbf{curl}, \Omega)$-conforming polynomials of degree at most p and $\{\lambda_j^\ell\}_{j,\ell}$ a basis of H^1-conforming polynomials of degree at most p^-. There holds,

$$k = 1: \qquad \mathrm{L}_{\mathbf{u}}^h \mathbf{w}_h = \mathcal{I}_{\mathbf{u},p}^1(\mathsf{i}_\mathbf{u}\mathsf{d}^1\mathbf{w}_h) + \mathsf{d}^0\,\mathcal{I}_{\mathbf{u},p^-}^0(\mathsf{i}_\mathbf{u}\mathbf{w}_h) = \mathcal{I}_{\mathbf{u},p}^1(\mathbf{curl}\,\mathbf{w}_h \times \mathbf{u}) + \operatorname{grad}(\mathcal{I}_{\mathbf{u},p^-}^0(\mathbf{u} \cdot \mathbf{w}_h))$$

$$= \sum_{j=1}^{M_{\min}^{p,1}} \sum_{f_j \in \Delta_j(\mathcal{T}_h)} \sum_{\ell=1}^{N_j} W_{f_j}^\ell((\mathbf{curl}\,\mathbf{w}_h \times \mathbf{u})^{\mathsf{upw}})\,\phi_j^\ell$$

$$+ \sum_{j=0}^{M_{\min}^{p^-,0}} \sum_{f_j \in \Delta_j(\mathcal{T}_h)} \sum_{\ell=1}^{N_j} W_{f_j}^\ell((\mathbf{u} \cdot \mathbf{w}_h)^{\mathsf{upw}})\operatorname{grad}\lambda_j^\ell,$$

$$(\mathbf{u} \cdot \mathbf{w}_h)^{\mathsf{upw}}(x) := \mathbf{u}(x) \cdot \mathbf{w}_{h|_{T_x^{\mathsf{upw}}}}(x), \qquad\qquad \forall\, x \in f_j \setminus \Gamma_{\mathrm{in}},$$

$$(\mathbf{curl}\,\mathbf{w}_h \times \mathbf{u})^{\mathsf{upw}}(x) := (\mathbf{curl}\,\mathbf{w}_h)_{|_{T_x^{\mathsf{upw}}}}(x) \times \mathbf{u}(x), \qquad \forall\, x \in f_j \setminus \Gamma_{\mathrm{in}},$$

and boundary conditions are used whenever $x \in \Gamma_{\mathrm{in}}$.

The representation in vector proxies of the Lie derivative of $k = 2$ and $k = 3$ can be derived analogously, using the correspondences between the exterior derivative and the contraction operator and the definition of the upwind interpolation $\mathcal{I}_{\mathbf{u},r}^2$ for $r \in \{p, p^-\}$.

Remark 2.5 (Tabata's scheme)**.** Let $\mathcal{T}_h$ denote a simplicial triangulation of $\Omega \subset \mathbb{R}^n$ of weakly acute type. We consider the extrusion contraction upwind discretization of the scalar advection problem with linear Lagrangian finite element spaces V_h. Using the discrete Lie derivative (2.18) in the weak formulation (2.17), yields the bilinear form

$$a_h(w_h, v_h) = \sum_{\ell=1}^{N_0} \mathbf{u}(x_\ell) \cdot (\operatorname{grad} w_h)_{|_{T_{x_\ell}^{\mathsf{upw}}}}(x_\ell) \int_\Omega \lambda^\ell v_h, \qquad \forall\, w_h, v_h \in V_h.$$

where $\{\lambda^\ell\}_\ell$ are the barycentric coordinates and $N_0 := \dim V_h = \sharp\Delta_0(\mathcal{T}_h)$. Approximating the integration on Ω using local quadrature rules $Q(T) = \{a_{i,T}, q_{i,T}\}_{i=0}^n$ with weights $\{q_{i,T} = 1/(n+1)\}_i$ and nodes $\{a_{i,T}\}_i$ at the mesh 0-cells (vertices of the n-simplices), results in

$$a_h(w_h, v_h) = \sum_{\ell=1}^{N_0} \mathbf{u}(x_\ell) \cdot (\operatorname{grad} w_h)_{|_{T_{x_\ell}^{\mathsf{upw}}}}(x_\ell) \sum_{T \in \mathcal{T}_h} \sum_{a_{i,T} \in \Delta_0(T)} q_{i,T}\lambda^\ell(a_{i,T})v_h(a_{i,T})$$

$$= \sum_{T \in \mathcal{T}_h} \sum_{a_{i,T} \in \Delta_0(T)} q_{i,T}\mathbf{u}(a_{i,T}) \cdot (\operatorname{grad} w_h)_{|_{T_{a_{i,T}}^{\mathsf{upw}}}}(a_{i,T})v_h(a_{i,T}),$$

and the so-called *upwind quadrature* or Tabata's scheme [38] is recovered. The method proposed by Tabata to solve the transient scalar advection-diffusion problem with homogeneous Dirichlet boundary conditions at the domain boundaries, is first order accurate, and it delivers an algebraic system M-matrix (i.e., a non-singular matrix whose entries $a_{i,j}$ satisfy $a_{i,j} \leq 0$ for $i \neq j$ and the entries $b_{i,j}$ of the inverse matrix are non-negative, $b_{i,j} \geq 0$). This entails that the discrete solution operator is inverse monotone. Therefore, when augmented with a standard linear finite element discretization of the diffusion operator, the resulting scheme is able to preserve the inverse-monotonicity property and hence the maximum principle characterizing the problem at the continuous level [38, Theorem 1].

2.4. Commuting Property of the Discrete Lie Derivative

Owing to Cartan's formula (2.10), it can be easily verified that the exterior derivative and the Lie derivative commute, namely

$$\mathsf{d}^k \mathsf{L}_{\mathbf{u}} \omega = \mathsf{L}_{\mathbf{u}} \mathsf{d}^k \omega, \qquad \forall\, \omega \in \Lambda^k\left(\Omega\right). \tag{2.19}$$

The commuting property has the fundamental consequence that closed differential forms are Lie advected into closed forms. In the MHD perspective, this corresponds to the fact that the $\mathbf{B}$ field is solenoidal at every time. Moreover, it entails that, if $\omega \in \Lambda^k\left(\Omega\right)$ is solution of the advection problem for k-forms, then $\mathsf{d}^k \omega$ is solution of the advection problem for $(k+1)$-forms, under suitable forcing terms, initial and boundary conditions. As an example, in three-dimensional ideal MHD flows, the magnetic potential $\mathbf{A}$ and the magnetic induction field, $\mathbf{B} = \mathbf{curl}\,\mathbf{A}$, satisfy the advection problem for the vector proxies of differential 1-forms and 2-forms, respectively.

The discretization of the Lie derivative proposed in (2.16) yields an advection operator satisfying the commuting property (2.19) in the discrete setting.

Proposition 2.6. *Let $\Omega \subset \mathbb{R}^n$ be a bounded Lipschitz domain and let $\mathcal{T}_h$ be a cellular complex on Ω. Let $p^+, r^+ \geq 1$ be such that $\mathsf{d}^k \Lambda_{h,p}^k\left(\mathcal{T}_h\right) \subset \Lambda_{h,p^+}^{k+1}\left(\mathcal{T}_h\right)$ and $\mathsf{d}^k \Lambda_{h,r}^k\left(\mathcal{T}_h\right) \subset \Lambda_{h,r^+}^{k+1}\left(\mathcal{T}_h\right)$, respectively, with $p, r \geq 1$. Let $\mathbf{u} \in W^{1,\infty}(\Omega)$ and let $\mathsf{L}_{\mathbf{u}}^h$ be the extrusion contraction upwind discretization of the Lie derivative $\mathsf{L}_{\mathbf{u}}$ in (2.16). For all $0 \leq k \leq n-1$, the following diagram*

$$
\begin{array}{ccc}
\Lambda_{0,r}^k\left(\mathcal{T}_h\right) & \xrightarrow{\ \mathsf{d}^k\ } & \Lambda_{h,r^+}^{k+1}\left(\mathcal{T}_h\right) \\
\Big\downarrow{\scriptstyle \mathsf{L}_{\mathbf{u}}^h} & & \Big\downarrow{\scriptstyle \mathsf{L}_{\mathbf{u}}^h} \\
\Lambda_{h,p}^k\left(\mathcal{T}_h\right) & \xrightarrow{\ \mathsf{d}^k\ } & \Lambda_{h,p^+}^{k+1}\left(\mathcal{T}_h\right),
\end{array}
$$

commutes, namely, $\mathsf{L}_{\mathbf{u}}^h \mathsf{d}^k \omega_h = \mathsf{d}^k \mathsf{L}_{\mathbf{u}}^h \omega_h$, for all $\omega_h \in \Lambda_{0,r}^k\left(\mathcal{T}_h\right) \subset H\Lambda^k\left(\Omega\right)$.

Proof. The commutativity of the discrete exterior and Lie derivatives follows immediately from the topological properties of the (discrete) exterior derivative. Indeed, if $\omega_h \in \Lambda_{h,r}^k\left(\mathcal{T}_h\right)$, the definition of discrete Lie derivative in (2.16) results in

$$\mathsf{L}_{\mathbf{u}}^h \mathsf{d}^k \omega_h = \mathcal{I}_{\mathbf{u},p^+}^{k+1}(\mathsf{i}_{\mathbf{u}} \mathsf{d}^{k+1} \mathsf{d}^k \omega_h) + \mathsf{d}^k\, \mathcal{I}_{\mathbf{u},p}^k(\mathsf{i}_{\mathbf{u}} \mathsf{d}^k \omega_h) = \mathsf{d}^k(\mathcal{I}_{\mathbf{u},p}^k(\mathsf{i}_{\mathbf{u}} \mathsf{d}^k \omega_h))$$

$$= \mathsf{d}^k(\mathsf{d}^{k-1} \mathcal{I}_{\mathbf{u},p^-}^{k-1}(\mathsf{i}_{\mathbf{u}} \omega_h) + \mathcal{I}_{\mathbf{u},p}^k(\mathsf{i}_{\mathbf{u}} \mathsf{d}^k \omega_h)) = \mathsf{d}^k \mathsf{L}_{\mathbf{u}}^h \omega_h,$$

owing to the fact that the discrete exterior derivative satisfies $\mathsf{d}^{k+1} \circ \mathsf{d}^k = 0$. ∎

The result of Proposition 2.6 has two major consequences. Under the assumption of unique solvability of the discrete time-dependent problem corresponding to (2.17), discrete closed k-forms are Lie advected into closed k-forms. Consider the semi-discrete problem $\partial_t \omega_h + \alpha \omega_h + \mathsf{L}_{\mathbf{u}}^h \omega_h = f$,

and suppose the initial datum is a closed form. From an algebraic perspective, let $\mathbb{L}$ be the matrix associated with the discretization of the Lie derivative (2.16). Let W^m be the vector of degrees of freedom for ω_h at time t^m. In the simplest case of explicit Euler timestepping, $\mathbb{M}W^{m+1} = \mathbb{M}W^m - \Delta t^m \alpha \mathbb{M}W^m - \Delta t^m \mathbb{L}W^m + \Delta t^m F^m$, where $\mathbb{M}$ is the mass matrix and F^m is the load vector associated with the source term at time t^m. By Proposition 2.6, the incidence matrix $\mathbb{D}^k$, representing the exterior derivative operator, commutes with $\mathbb{L}$. Hence, under suitable boundary conditions, $\mathbb{D}^k W^m = 0$ for all $m \geq 1$, provided the right hand side is closed at all times. Secondly, the polynomial spaces $\mathcal{P}_r^- \Lambda^k(\mathcal{T}_h)$ and $\mathcal{Q}_r^- \Lambda^k(\mathcal{T}_h)$ form long exact sequences for a fixed polynomial degree $r \geq 1$ [3, Section 3.5]. If a priori convergence results (in a certain norm) independent of the form degree k can be established, then, upon suitably tuning the polynomial approximation and interpolation orders, no accuracy is lost in solving the advection problem for the magnetic potential, rather than the magnetic induction advection.

Remark 2.7 (Discontinuous velocity). Inevitable shock formation in compressible MHD requires us to deal with the Lie advection associated with discontinuous velocities. In the presence of velocity fields with very low regularity, well-posedness results for the generalized advection equations and a notion of generalized flow maps are largely unavailable. However, provided a discrete velocity field $\mathbf{u}_h$ can be uniquely defined at the mesh facets, e.g. through consistent averaging, the upwind interpolation of contraction and hence a discrete Lie derivative associated with $\mathbf{u}_h$ can be derived. In this setting, the discrete commuting diagram property does still hold. In the context of MHD, local wave speeds offer a way of uniquely defining a velocity at faces where an upwind direction cannot be determined from $\mathbf{u}$, see Remark 4.1 for details.

3. Extended Euler Equations

The local splitting of the MHD system yields an advection problem for the magnetic induction/potential with a known discontinuous velocity field, and the extended Euler system of conservation laws for the fluid variables with the $\mathbf{B}$ field treated as a discontinuous known function. Using standard vector identities, see e.g. [15, Section 2.4.1 and Appendix A.1], the evolution equations for the fluid variables (1.1a)-(1.1c) reduce to the fluid part of the ideal MHD equations written in conservation form, namely

$$\begin{cases} \partial_t \rho + \operatorname{div}(\rho \mathbf{u}) = 0, \\ \partial_t(\rho \mathbf{u}) + \mathbf{div}\left(\rho \mathbf{u} \otimes \mathbf{u} + \left(p + \frac{1}{2}\|\mathbf{B}\|_{L^2}^2\right)\mathbb{I} - \mathbf{B} \otimes \mathbf{B}\right) = \mathbf{0}, \\ \partial_t E + \operatorname{div}\left(\left(E + p + \frac{1}{2}\|\mathbf{B}\|_{L^2}^2\right)\mathbf{u} - (\mathbf{u} \cdot \mathbf{B})\mathbf{B} + \varepsilon \,\mathbf{curl}\mathbf{B} \times \mathbf{B}\right) = 0. \end{cases} \tag{3.1}$$

The extended Euler system is a *parametric* hyperbolic system of conservation laws. In three dimensions, if $\mathbf{U} := (\rho, \rho u^1, \rho u^2, \rho u^3, E)$ denotes the vector of the conserved fluid variables, and $\mathbf{x} = (x^1, x^2, x^3) \in \mathbb{R}^3$, then (3.1) can be written in conservation form according to (1.1) as

$$\partial_t \mathbf{U} + \sum_{\ell=1}^3 \partial_{x^\ell} f^\ell(\mathbf{U}, \mathbf{B}) = \mathbf{0}. \tag{3.2}$$

If $\delta_{i,\ell}$ denotes the Kronecker delta, the directional fluxes $\{f^\ell\}_{\ell=1}^3$ are defined as

$$f^\ell(\mathbf{U}, \mathbf{B}) = \begin{pmatrix} \rho u^\ell \\ \rho u^1 u^\ell - B_1 B_\ell + \left(p + \frac{1}{2}\|\mathbf{B}\|_{L^2}^2\right)\delta_{1,\ell} \\ \rho u^2 u^\ell - B_2 B_\ell + \left(p + \frac{1}{2}\|\mathbf{B}\|_{L^2}^2\right)\delta_{2,\ell} \\ \rho u^3 u^\ell - B_3 B_\ell + \left(p + \frac{1}{2}\|\mathbf{B}\|_{L^2}^2\right)\delta_{3,\ell} \\ \left(E + p + \frac{1}{2}\|\mathbf{B}\|_{L^2}^2\right)u^\ell - (\mathbf{u} \cdot \mathbf{B})B_\ell \end{pmatrix}.$$

The extended Euler equations form a weakly hyperbolic system of conservation laws. In order to draw information on the spectral structure of the system, one can derive, as in [14, Section 2.1], a quasi-linear form of (3.2) in the primitive variables unknowns $\mathbf{V} := (\rho, u^1, u^2, u^3, p)$, namely

$$\partial_t \mathbf{V} + \sum_{\ell=1}^{3} A^\ell(\mathbf{V}, \mathbf{B}) \partial_{x^\ell} \mathbf{V} = S(\mathbf{V}, \mathbf{B}, D\mathbf{B}),$$

where the right hand side S might depend on the induction field $\mathbf{B}$ and its Jacobian $D\mathbf{B}$. The directional Jacobian $\mathbf{A}(\mathbf{V}, \mathbf{B}) \cdot \mathbf{n} := \sum_{\ell=1}^{3} A^\ell(\mathbf{V}, \mathbf{B}) n_\ell$ in the direction of the unit vector $\mathbf{n} = (n_1, n_2, n_3)$ is given by

$$\mathbf{A}(\mathbf{V}, \mathbf{B}) \cdot \mathbf{n} = \begin{pmatrix} \mathbf{u} \cdot \mathbf{n} & \rho n_1 & \rho n_2 & \rho n_3 & 0 \\ 0 & \mathbf{u} \cdot \mathbf{n} & 0 & 0 & 1/\rho n_1 \\ 0 & 0 & \mathbf{u} \cdot \mathbf{n} & 0 & 1/\rho n_2 \\ 0 & 0 & 0 & \mathbf{u} \cdot \mathbf{n} & 1/\rho n_3 \\ 0 & \rho(a^{\mathrm{E},1}(\mathbf{V}, \mathbf{B}))^2 & \rho(a^{\mathrm{E},2}(\mathbf{V}, \mathbf{B}))^2 & \rho(a^{\mathrm{E},3}(\mathbf{V}, \mathbf{B}))^2 & \mathbf{u} \cdot \mathbf{n} \end{pmatrix},$$

where the sound speeds of the acoustic waves of the extended Euler system in each direction are

$$a^{\mathrm{E},\ell}(\mathbf{V}, \mathbf{B}) = \frac{1}{\sqrt{\rho}} \sqrt{\gamma p n_\ell + (\gamma - 1) \left[n_\ell(\|\mathbf{B}\|_{L^2}^2 - B_\ell^2) - B_\ell(\mathbf{B} \cdot \mathbf{n} - B_\ell n_\ell) \right]}, \qquad \ell \in \{1, 2, 3\}. \qquad (3.3)$$

If $\mathbf{u}^{\mathrm{E}} := (a^{\mathrm{E},1}(\mathbf{V}, \mathbf{B}), a^{\mathrm{E},2}(\mathbf{V}, \mathbf{B}), a^{\mathrm{E},3}(\mathbf{V}, \mathbf{B}))$, the eigenvalues of the directional Jacobian are

$$\lambda^1 = \mathbf{u} \cdot \mathbf{n} - \mathbf{u}^{\mathrm{E}} \cdot \mathbf{n}, \qquad \lambda^{2,3,4} = \mathbf{u} \cdot \mathbf{n}, \qquad \lambda^5 = \mathbf{u} \cdot \mathbf{n} + \mathbf{u}^{\mathrm{E}} \cdot \mathbf{n}. \qquad (3.4)$$

The Riemann solution of the extended Euler system is then characterized by five waves: two acoustic waves, rarefactions/shocks moving to the left/right and a shear wave.

3.1. **Finite Volume Discretization**

For the numerical discretization of the extended Euler problem, we design, in the present section, finite volume schemes using reduced waves approximate Riemann solvers as in [14, Section 2.1].

For the sake of simplicity, hereafter we restrict to Cartesian domains $\Omega = J_1 \times \ldots \times J_n \subset \mathbb{R}^n$, with $J_\ell \subset \mathbb{R}$, $\ell = 1, \ldots, n$, bounded and connected, and to tensor product partitions $\{\mathcal{T}_h\}_h$ of Ω. We assume that $\mathcal{T}_{h_\ell}^\ell$ is a uniform mesh on J_ℓ with $M_h^\ell := \sharp \mathcal{T}_{h_\ell}^\ell$ elements and mesh width $h_\ell = |J_\ell|/M_h^\ell$. Every control volume $T_{\mathsf{j}} \in \mathcal{T}_h$ is identified by its barycenter $\mathbf{x}_{\mathsf{j}} = (x_{j_1}^1, \ldots, x_{j_n}^n)$, where $\mathsf{j} = (j_1, \ldots, j_n)$ is a multi-index in $\mathfrak{J} := \mathbb{N}^n \cap ([1, M_h^1] \times \ldots \times [1, M_h^n])$. The interfaces of the element $T_{\mathsf{j}} \in \mathcal{T}_h$ are denoted by $\mathbf{x}_{\mathsf{j}+\frac{1}{2}\mathbf{e}_{\mathsf{t}}}$ where $\mathbf{e}_{\mathsf{t}}$ is the t-th unit vector in $\mathbb{R}^n$.

The weak solution $\mathbf{U}(\mathbf{x}, t)$ of the extended Euler system is approximated by cell averages,

$$\mathbf{U}(\mathbf{x}, t)_{|T_{\mathsf{j}}} \approx \mathbf{U}_{\mathsf{j}}(t) := \frac{1}{|T_{\mathsf{j}}|} \int_{T_{\mathsf{j}}} \mathbf{U}(\mathbf{x}, t) d\mathbf{x}, \qquad \forall T_{\mathsf{j}} \in \mathcal{T}_h, \mathsf{j} \in \mathfrak{J}.$$

A semi-discrete finite volume scheme for the conservation law (3.2) on a fixed element $T_{\mathsf{j}} \in \mathcal{T}_h$ is given by

$$\partial_t \mathbf{U}_{\mathsf{j}}(t) = -\sum_{\ell=1}^{n} \frac{F_{\mathsf{j}+\frac{1}{2}\mathbf{e}_\ell}^\ell(t) - F_{\mathsf{j}-\frac{1}{2}\mathbf{e}_\ell}^\ell(t)}{h_\ell}, \qquad \forall \mathsf{j} \in \mathfrak{J},$$

where $F_{\mathsf{j}+\frac{1}{2}\mathbf{e}_\ell}^\ell(t) = F_{\mathsf{j}+\frac{1}{2}\mathbf{e}_\ell}^\ell(\mathbf{B}(\mathbf{x}_{\mathsf{j}+\frac{1}{2}\mathbf{e}_\ell}, t), t)$ is a numerical flux consistent with the directional flux f^ℓ.

The temporal interval I is divided into subintervals $I = \bigcup_{m=0}^{N-1} (t^m, t^{m+1}]$, $N \in \mathbb{N}$, with $t^{m+1} = t^m + \Delta t^m$. The temporal discretization is based on explicit *strong-stability preserving* Runge–Kutta (SSP-RK) schemes [16]. Concerning the choice of the time step, we adopt a perspective where the extended Euler equations are considered as embedded in the physics of the full ideal MHD system.

237

Since in MHD the fast magnetosonic waves propagate on a time scale much faster than the fluid velocity, these waves dictate the time step restrictions necessary for a stable numerical update. For the temporal discretization of the extended Euler system, the m-th time step is taken to be

$$\Delta t^m = C_{\text{CFL}} \left(\sum_{\ell=1}^{n} \frac{\lambda_{\max}^{\ell,m}}{h_\ell} \right)^{-1},$$

where $C_{\text{CFL}} > 0$ is a constant and $\{\lambda_{\max}^{\ell,m}\}_{\ell=1}^{n}$ are the maximum eigenvalues associated with the fast magnetosonic waves, namely

$$\lambda_{\max}^{\ell,m} = \max_{\mathsf{j} \in \mathcal{J}} (|u_{\mathsf{j}}^{\ell,m}| + c_f^{\text{M},\ell}(\mathbf{U}_{\mathsf{j}}^m, \mathbf{B}_{\mathsf{j}}^m)), \qquad\qquad \ell = 1, \ldots, n,$$

$$c_f^{\text{M},\ell}(\mathbf{U}, \mathbf{B}) = \frac{1}{\sqrt{2}} \sqrt{a^2 + \frac{\|\mathbf{B}\|_{L^2}^2}{\rho} + \sqrt{\left(a^2 + \frac{\|\mathbf{B}\|_{L^2}^2}{\rho} \right)^2 - 4a^2 \frac{B_\ell^2}{\rho}}}, \qquad \ell = 1, \ldots, n. \qquad (3.5)$$

3.1.1. *Approximate Riemann Solvers*

Reduced-wave nonlinear solvers, the so-called *HLL solvers*, approximate the wave structure of the full Riemann problem by a simplified set of known waves and provide an accurate and computationally efficient alternative to the use of Roe-type linearized Riemann solvers [9]. For the sake of better readability, in the following only the $x := x^1$-direction is considered, the superscript $\ell = 1$ is omitted and we switch from the multi-index j to the index i treating the problem as one-dimensional.

Two-wave HLL Solver. The Harten–Lax–van Leer (HLL) approximate Riemann solver, introduced in [20] for the inviscid gas dynamic equations, assumes a wave configuration for the Riemann problem solution consisting of three constant states separated by two shock waves moving to the left and to the right of the interface. The resulting HLL flux solver at time t^m is

$$F_{i+1/2}^{m,\text{HLL}} = F(\mathbf{U}_i^m, \mathbf{U}_{i+1}^m, \mathbf{B}_{i+1/2}^m) = \begin{cases} f(\mathbf{U}_i^m, \mathbf{B}_{i+1/2}^m) & \text{if } s_{i+1/2}^L > 0, \\ f_{i+1/2}^{*,\text{HLL}} & \text{if } s_{i+1/2}^L < 0 < s_{i+1/2}^R, \\ f(\mathbf{U}_{i+1}^m, \mathbf{B}_{i+1/2}^m) & \text{if } s_{i+1/2}^R < 0. \end{cases}$$

The selection of the left $s_{i+1/2}^L$ and right $s_{i+1/2}^R$ acoustic wave speeds determines different variants of the approximate flux. The middle flux $f_{i+1/2}^{*,\text{HLL}}$ is determined, together with the intermediate subsonic state $\mathbf{U}_{i+1/2}^*$, by applying local conservation through Rankine–Hugoniot conditions, namely

$$f(\mathbf{U}_{i+1}^m, \mathbf{B}_{i+1/2}^m) - f_{i+1/2}^{*,\text{HLL}} = s_{i+1/2}^R(\mathbf{U}_{i+1}^m - \mathbf{U}_{i+1/2}^*),$$
$$f_{i+1/2}^{*,\text{HLL}} - f(\mathbf{U}_i^m, \mathbf{B}_{i+1/2}^m) = s_{i+1/2}^L(\mathbf{U}_{i+1/2}^* - \mathbf{U}_i^m).$$

Note that the computation of the flux $f(\mathbf{U}_i^m, \mathbf{B}_{i+1/2}^m)$ requires the knowledge of both the tangential and normal components of the $\mathbf{B}$ field at the interface. Whenever one of these quantities is not uniquely defined, we will take the arithmetic average $\{B_1\}_{i+1/2}$ and/or $\{B_2\}_{i+1/2}$ across the interface.

To determine the right and left speeds, Einfeldt suggested in [11] to use the minimum and maximum eigenvalues of a Roe average to restrain the spreading of contact discontinuities and increase the resolution at isolated shocks. Lacking a Roe average for the extended Euler system, we take the right and left speeds as,

$$s_{i+1/2}^L := \min\{u_i^{1,m} - a^{\text{E},1}(\mathbf{V}_i^m, \mathbf{B}_i^m), \{u^{1,m}\}_{i+1/2} - \widehat{a}^{\text{E},1}(\{\mathbf{V}^m\}_{i+1/2}, \{\mathbf{B}^m\}_{i+1/2})\},$$
$$s_{i+1/2}^R := \max\{u_{i+1}^{1,m} + a^{\text{E},1}(\mathbf{V}_{i+1}^m, \mathbf{B}_{i+1}^m), \{u^{1,m}\}_{i+1/2} + \widehat{a}^{\text{E},1}(\{\mathbf{V}^m\}_{i+1/2}, \{\mathbf{B}^m\}_{i+1/2})\},$$

$$(3.6)$$

where $\{u^{1,m}\}_{i+1/2}$ is the arithmetic average of the normal velocity and $\widehat{a}^{E,1}$ is the sound speed of the acoustic wave of the extended Euler system (in the x^1-directions) associated with the (arithmetic) averaged directional Jacobian

$$\widehat{A}^1_{i+1/2} = \begin{pmatrix} \{u^{1,m}\}_{i+1/2} & \{\rho^m\}_{i+1/2} & 0 & 0 & 0 \\ 0 & \{u^{1,m}\}_{i+1/2} & 0 & 0 & \{1/\rho^m\}_{i+1/2} \\ 0 & 0 & \{u^{1,m}\}_{i+1/2} & 0 & 0 \\ 0 & 0 & 0 & \{u^{1,m}\}_{i+1/2} & 0 \\ 0 & \{\rho^m(a^{E,1})^2\}_{i+1/2} & \{\rho^m(a^{E,2})^2\}_{i+1/2} & \{\rho^m(a^{E,3})^2\}_{i+1/2} & \{u^{1,m}\}_{i+1/2} \end{pmatrix}.$$

Analogously to $a^{E,1}$ in (3.3), the speed $\widehat{a}^{E,1}$ is defined as

$$(\widehat{a}^{E,1})^2 = \left\{\frac{1}{\rho^m}\right\}_{i+1/2} \left\{\rho^m(a^{E,1})^2\right\}_{i+1/2}$$
$$= \left(\frac{1}{\rho_i^m} + \frac{1}{\rho_{i+1}^m}\right)\left(\gamma(p_i^m + p_{i+1}^m) + (\gamma-1)[(B_2^m)_i^2 + (B_2^m)_{i+1}^2 + (B_3^m)_i^2 + (B_3^m)_{i+1}^2]\right).$$

Despite the efficiency and robustness of HLL-type Riemann solvers, the two-wave configuration hinders the resolution of physical features, in particular Alfvén and slow waves and contact discontinuities, yielding overdiffusive solutions.

Three-wave HLLC Solver. Contact discontinuities are "restored" in the modified HLL solver introduced by Toro, Spruce and Speares [39] and dubbed HLLC. The HLLC solver approximates the Riemann solution by three waves allowing for two intermediate states. The fast magnetosonic waves are modeled as in the HLL solver, whilst the intermediate states are separated by a wave moving with speed $s^M_{i+1/2}$ and modeling a contact discontinuity (associated with the multiple eigenvalue $\lambda^{2,3,4}$ (3.4)). The HLLC numerical flux is defined as

$$F^{m,\text{HLLC}}_{i+1/2} = F(\mathbf{U}_i^m, \mathbf{U}_{i+1}^m, \mathbf{B}^m_{i+1/2}) = \begin{cases} f(\mathbf{U}_i^m, \mathbf{B}^m_{i+1/2}) & \text{if } s^L_{i+1/2} > 0, \\ f_L^* & \text{if } s^L_{i+1/2} < 0 < s^M_{i+1/2}, \\ f_R^* & \text{if } s^M_{i+1/2} < 0 < s^R_{i+1/2}, \\ f(\mathbf{U}_{i+1}^m, \mathbf{B}^m_{i+1/2}) & \text{if } s^R_{i+1/2} < 0. \end{cases}$$

The left and right speeds model the fast magnetosonic waves and are as in (3.6), the middle wave speed $s^M_{i+1/2}$ is the velocity of the averaged Jacobian $s^M_{i+1/2} = \{u^{1,m}\}_{i+1/2}$ since it models the contact discontinuity. The intermediate fluxes are determined by applying local conservation through the Rankine–Hugoniot conditions

$$s^L_{i+1/2}\mathbf{U}_L^* - f_L^* = s^L_{i+1/2}\mathbf{U}_i^m - f(\mathbf{U}_i, \mathbf{B}^m_{i+1/2}),$$
$$s^M_{i+1/2}\mathbf{U}_L^* - f_L^* = s^M_{i+1/2}\mathbf{U}_R^* - f_R^*, \tag{3.7}$$
$$s^R_{i+1/2}\mathbf{U}_{i+1}^m - f(\mathbf{U}_{i+1}^m, \mathbf{B}^m_{i+1/2}) = s^R_{i+1/2}\mathbf{U}_R^* - f_R^*,$$

where $\mathbf{U}_R^*$ and $\mathbf{U}_L^*$ denote the right and left intermediate states, respectively. Simple algebraic manipulations yield the intermediate fluxes f_R^* and f_L^*. However, since the system (3.7) is underdetermined, a further constraint on the intermediate states needs to be imposed. Linde suggested in [29, Section 4.3.3] to compute the jump of the intermediate states as a non-negative fraction of the initial jump across the middle wave, namely $\mathbf{U}_R^* - \mathbf{U}_L^* = \alpha(\mathbf{U}_i^m - \mathbf{U}_{i+1}^m)$ for $\alpha \in [0,1]$. If $c_* := |a^{E,1}(V_i^m, \mathbf{B}_i^m) - s^M_{i+1/2}|$, the choice

$$\alpha = \max\left\{0, 1 - \frac{s}{c_*}\right\}, \quad s := \frac{\|f(\mathbf{U}_{i+1}^m, \mathbf{B}^m_{i+1/2}) - f(\mathbf{U}_i^m, \mathbf{B}^m_{i+1/2}) - s^M_{i+1/2}(\mathbf{U}_{i+1}^m - \mathbf{U}_i^m)\|_{\ell^1}}{\left\|\mathbf{U}_{i+1}^m - \mathbf{U}_i^m\right\|_{\ell^1}},$$

aims at robustness of the Riemann solver together with good resolution of isolated shocks. As pointed out in [29], s gives an indication of the speed of the dominant wave in the frame of reference of the middle wave. Note that s can be in principle computed using a different norm.

3.1.2. *Limitations of Finite Volume Schemes for the Extended Euler System*

The formulation of approximate Riemann solvers for the extended Euler equations based on HLL-type solvers for the MHD Riemann problem is an attempt to capture the wave structure of the reduced problem viewed as a subset of the ideal MHD wave fan. However, the good properties of the aforementioned approximate Riemann solvers for the MHD system are not inherited straightforwardly by the extended Euler equations. As pointed out in [14], the lack of control on the $\mathbf{B}$ field and the unavailability of a Roe average, which consequently affects the choice of the wave speeds, do not guarantee that the resulting scheme is able to exactly capture fast magnetosonic shocks or isolated contact discontinuities. Analogously, with the $\mathbf{B}$ field resulting from the extrusion contraction approximation (2.16) of the magnetic advection problem for the magnetic field/potential, none of the foregoing solvers for the extended Euler system is provably positively conservative. Furthermore, the presence of the $\mathbf{B}$ field as a parameter entering the fluxes hinders the design of numerical fluxes satisfying a discrete version of the entropy inequality $\partial_t(\rho s) + \mathrm{div}(\rho \mathbf{u} s) \leq 0$, where $s := \log(p) - \gamma \log(\rho)$ is the thermodynamic entropy.

3.2. **Fully Coupled FV-FEEC Schemes**

The extrusion contraction upwind discretization derived in Section 2 for the magnetic induction equation and the finite volume schemes for the extended Euler system described in Section 3 can be combined in numerical schemes for the full ideal MHD problem, which we coin FV-FEEC (Finite Volume-Finite Element Exterior Calculus).

We implement a *synchronous* splitting, Algorithm 1, where the two systems, extended Euler and magnetic advection, are concurrently advanced in time, in the sense that after spatial discretization, the two problems are re-coupled to form a single system of ODEs. The latter is solved via explicit SSP Runge–Kutta timestepping. In this way, the coupling fields, the velocity and the magnetic induction, are updated within each subsystems at every intermediate stage of the temporal scheme.

Algorithm 1 Synchronous splitting algorithm

1: Set $m = 0$, $t = 0$. Given initial conditions $(\rho_0, \mathbf{u}_0, E_0, \mathbf{B}_0)$.
2: **while** time $t < T$ **do**
3:     $\mathbf{u}^{m;0} = \mathbf{u}^m$; $\mathbf{B}^{m;0} = \mathbf{B}^m$.
4:     **for** each stage $1 \leq i \leq s$ of an s-stage SSP-RK timestepping **do**
5:         $\begin{pmatrix} \mathbf{u}^{m;i} \\ \mathbf{A}^{m;i} \end{pmatrix} \longleftarrow$ Solve extended Euler and advection of $(n-2)$-forms given $\left\{ \begin{pmatrix} \mathbf{B}^{m;j} \\ \mathbf{u}^{m;j} \end{pmatrix} \right\}_{j=0}^{i-1}$.
6:         $\mathbf{B}^{m;i} \longleftarrow$ Compute the (discrete) curl of $\mathbf{A}^{m;i}$.
7:     **end for**
8:     $\mathbf{u}^{m+1} = \mathbf{u}^{m;s}$; $\mathbf{A}^{m+1} = \mathbf{A}^{m;s}$; $\mathbf{B}^{m+1} = \mathbf{B}^{m;s}$.
9:     Set $t = t + \Delta t^m$, $m = m + 1$.
10: **end while**

---

4. Numerical Experiments in Two Dimensions

This section is devoted to testing the new family of FV-FEEC schemes for the two-dimensional planar MHD problem. The aim is to provide numerical evidence of their accuracy, good stability properties and ability in preserving the physical distinctive features of the model at the continuous level. The two-dimensional setting provides a first step to assess the robustness of numerical schemes maintaining many of the physical features of the three-dimensional model.

Lacking a stability and convergence theory for the extrusion contraction upwind schemes, we first test the method introduced in Section 2.2 for the transient advection problem. The aim is to derive empiric convergence properties in the L^2-norm and in some energy norm, and to look for numerical confirmation of the discrete commuting property stated in Proposition 2.6.

4.1. **Numerical Tests: Extrusion Contraction**

Since we are interested in the transient advection problem as part of the planar two-dimensional MHD model, we restrict to numerical simulations for the advection of 0-forms and 1-forms in two dimensions. Note that in this case the magnetic potential is a scalar function representing the transverse out-plane component of the three-dimensional vector magnetic potential, $\mathbf{B} = \mathbf{curl}_{2D} A := (\partial_y A, -\partial_x A)^\top$.

4.1.1. *Transient Advection of 0-Forms*

On the domain $\Omega = [0,2]^2$ and on the time interval $I = [0,T] \subset \mathbb{R}$, $T > 0$, we consider the pure advection problem for the scalar magnetic potential A, namely

$$\begin{aligned} \partial_t A(t) + \mathbf{u} \cdot \mathrm{grad} A(t) = 0, & \quad \text{in } \Omega \times I, \\ A(0) = A_0, & \quad \text{in } \Omega, \end{aligned} \tag{4.1}$$

with periodic boundary conditions.

Test of Convergence: Constant Velocity. The initial condition $A_0 = \frac{1}{\pi} \cos(\pi y) + \frac{1}{2\pi} \cos(2\pi x)$ is advected at constant velocity $\mathbf{u} = (4,4)^\top$. On a family of Cartesian meshes $\{\mathcal{T}_h\}_h$, we consider the discrete variational formulation (2.17) with approximation spaces $\Lambda_{h,r}^0 (\mathcal{T}_h)$ of bilinear ($r = 1$) and biquadratic ($r = 2$) Lagrangian finite elements. The polynomial degree of the upwind interpolation is chosen to coincide with the polynomial degree of the finite element trial and test spaces, that is $p = r$ in (2.18). In order to gauge the spatial accuracy of the extrusion contraction scheme, we use Heun timestepping with uniform time step $\Delta t = 0.1h$ for bilinear Lagrangian finite element approximations and $\Delta t = 0.01h$ for biquadratic Lagrangian finite elements. Owing to the periodicity of the domain, we can compare the numerical solution at final time $T = 0.5$ with A_0.

The projection of the numerical and exact solution at final time onto the one-dimensional line $\{\mathbf{x} \in \Omega, y = 1\}$ is shown in Figure 4.1, bottom row. The piecewise linear discretization yields a rather diffusive solution and first order accuracy in both the L^2- and H^1-norms, as reported in Figure 4.1 where the L^2-error of the potential A and of its two-dimensional $\mathbf{curl}$, the magnetic induction field $\mathbf{B}$, is reported. Second order convergence is attained in the case of piecewise biquadratic discretization (and interpolation).

Orszag–Tang Benchmark with Given Velocity Field. We assess the performance of the extrusion contraction scheme in solving the more challenging MHD problem given by the Orszag–Tang vortex system [32] (see Section 4.3.3 for further details). We consider problem (4.1) with initial magnetic potential $A_0 = \frac{1}{\pi} \cos(\pi y) + \frac{1}{2\pi} \cos(2\pi x)$. The velocity field is supplied at each time step as the output
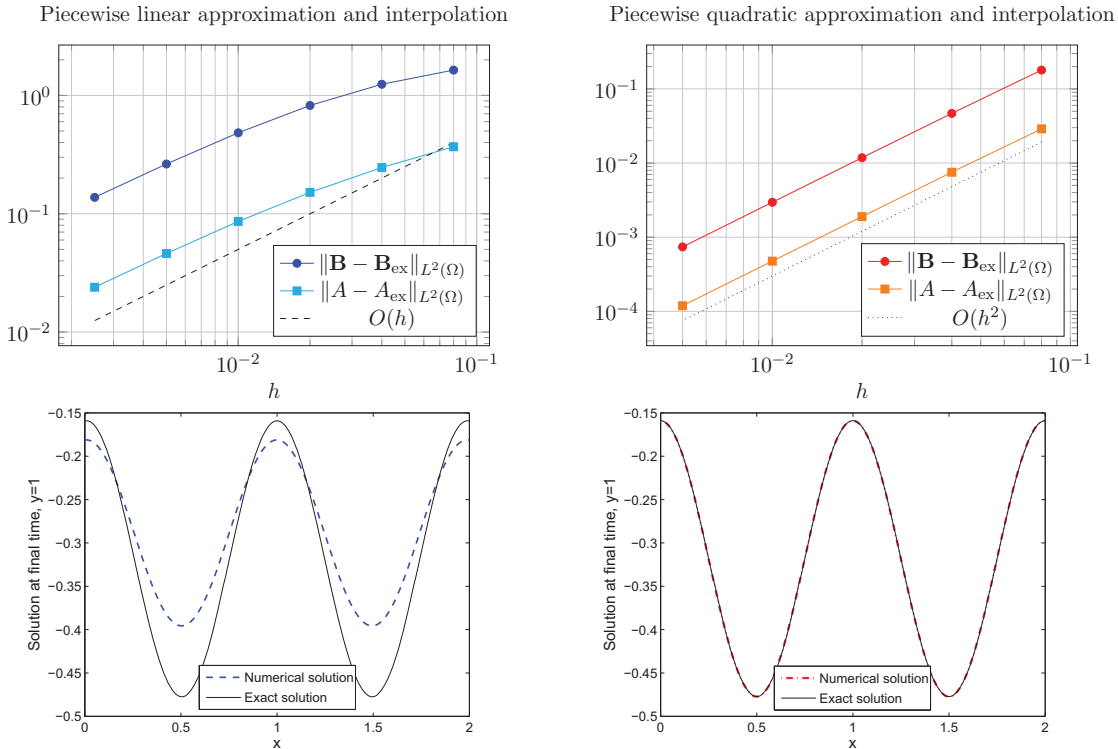
Figure 4.1. Test for advection of 0-forms with constant velocity. Convergence plot of the error in the L^2-norm at time $t = 0.5$ for the magnetic potential A and the induction field $\mathbf{B}$ (top row). The exact solution is $A_{\text{ex}} \equiv A_0$ and analogous for the $\mathbf{B}$ field. Projection of the exact and numerical solution for $y = 1$ on a 200×200 Cartesian mesh (bottom row). Left: first order interpolation, bilinear Lagrangian finite elements. Right: second order interpolation, biquadratic Lagrangian finite elements.

of a high order finite volume discretization of the full ideal MHD system obtained with the ALSVID-UQ 3.0 (2014-03-20) code[1] (using a three-wave HLL solver and WENO reconstructions modified in order to keep the pressure and density positive).

The scalar advection problem is discretized in space on a Cartesian mesh using extrusion contraction piecewise linear and piecewise quadratic upwind schemes with velocity field averaged at the interpolation nodes and upwind direction at each node given by the averaged velocity (in MHD flow simulations a more sophisticated approach to avoid the possible shortcoming of averaging the velocity values will be pointed out in Section 4.3). The polynomial order of the upwind interpolation operator coincides with the polynomial approximation degree. Heun timestepping is used for the temporal approximation on the time interval $I = [0, 1]$ with uniform time step $\Delta t = 5 \cdot 10^{-4}$.

The projection of the magnetic induction field, obtained with the foregoing discretizations, on lines at constant x is compared with the reference finite volume discrete solution in Figure 4.2. As expected, the piecewise quadratic extrusion contraction approximation produces more accurate solutions than the piecewise linear discretization. Obviously, near shocks and discontinuities, the piecewise quadratic solution exhibits "overshoots" and "undershoots". This is a typical by-product of numerical discretizations higher than first order accurate, as symptom of lack of monotonicity. We will comment on this issue later in Section 5.

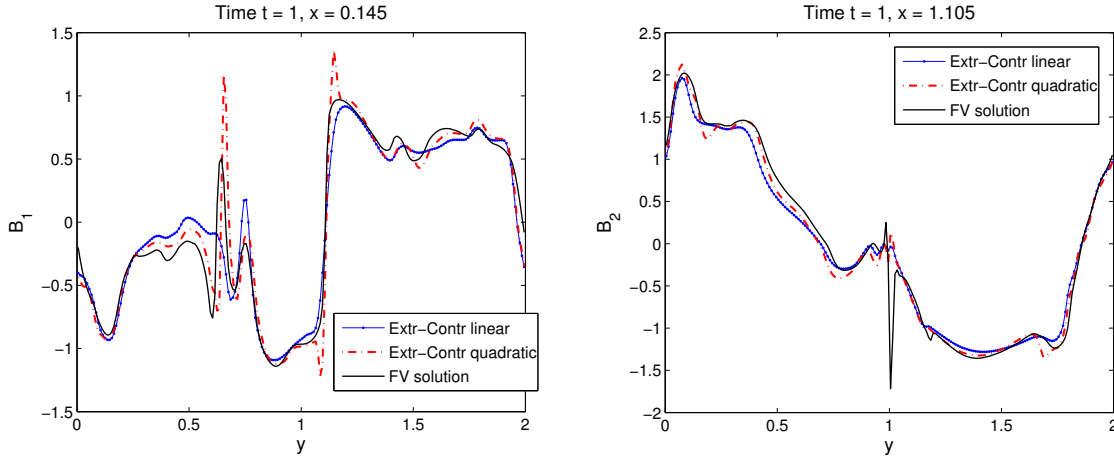[1] http://www.sam.math.ethz.ch/alsvid-uq (Accessed March 2016)

FIGURE 4.2. Orszag–Tang benchmark with given velocity field. Comparison plots of the projection of the $\mathbf{B}$ field for constant values of the x-coordinate on a Cartesian mesh with 200×200 elements. Discretization of the advection problem for 0-forms using piecewise linear and piecewise quadratic extrusion contraction upwind schemes. As "reference" solution, a high order finite volume solution of the full ideal MHD system obtained with the ALSVID-UQ code is considered.

4.1.2. *Transient Advection of* 1-*Forms*

On a simply connected bounded domain $\Omega \subset \mathbb{R}^2$ with Lipschitz boundary, we address the discretization of the initial boundary value problem describing the advection of the magnetic induction

$$\partial_t \mathbf{B} + \mathbf{u}\,\mathrm{div}\mathbf{B} + \mathrm{grad}^{\perp}(\mathbf{B} \cdot \mathbf{u}) = \mathbf{f}, \qquad \text{in } \Omega \times I,$$
$$\mathbf{B}(0) = \mathbf{B}_0, \quad \text{in } \Omega, \tag{4.2}$$

with periodic boundary conditions and where $\perp$ denotes a clockwise rotation of $\pi/2$. We consider lowest order finite element approximations with finite element spaces of polynomial discrete differential forms of the first family, namely the rotated Raviart-Thomas elements [34].

Test of Convergence: Constant Velocity. The goal of this experiment is twofold: infer the possible accuracy of the scheme and verify that solenoidal vector fields are indeed advected into solenoidal vector fields, as asserted in Proposition 2.6. The magnetic advection problem (4.2) is considered on the domain $\Omega = [0, 2]^2$ with periodic boundary conditions and in the time interval $I = [0, 0.5]$. The initial condition is set to $\mathbf{B}_0 = (-\sin(\pi y), \sin(2\pi x))^{\top}$, the velocity is constant $\mathbf{u} = (4, 4)^{\top}$ and the forcing term vanishes $\mathbf{f} = (0, 0)^{\top}$. In view of the periodic boundary conditions, we compare the solution at final time with the initial condition. Figure 4.3 shows that the L^2-error converges with order one with respect to the mesh width h and the divergence of the magnetic induction field is maintained zero up to machine precision.

Advection of Non-Solenoidal Magnetic Induction. As a second test case, we consider the advection of a magnetic induction field with non-zero divergence with the aim of monitoring the convergence rate of the solution in the L^2-norm and in the energy norm. On the unit square $\Omega = [0, 1]^2$ with periodic boundary conditions and in the time interval $I = [0, 0.5]$, we consider the magnetic advection problem (4.2) with initial condition given by

$$\mathbf{B}_0 := \begin{cases} (\varphi, \varphi)^{\top} & \text{if } x^2 + (y - 0.25)^2 < 0.25, \\ (0, 0)^{\top} & \text{otherwise,} \end{cases}$$

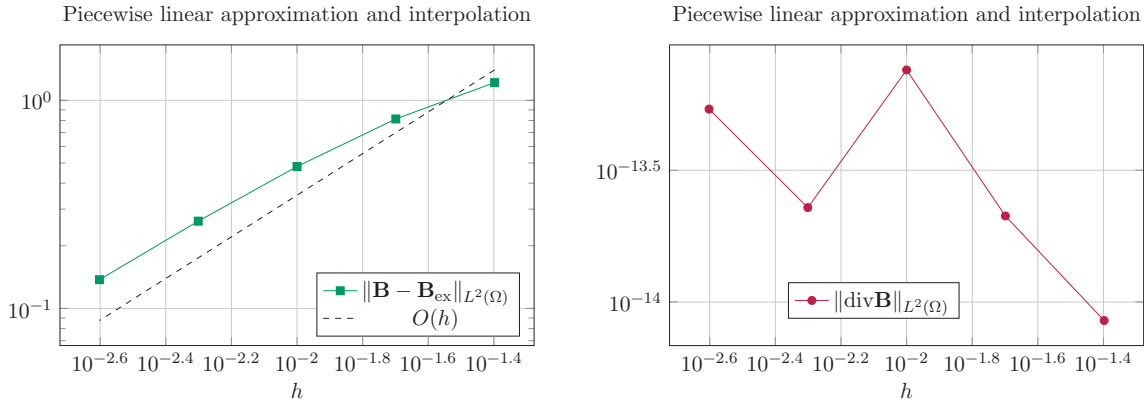Piecewise linear approximation and interpolation   Piecewise linear approximation and interpolation

FIGURE 4.3. Test for advection of 1-forms with constant velocity. Convergence plot of the error in the L^2-norm at final time $T = 0.5$ (left). L^2-norm of the magnetic induction field (right). Piecewise linear extrusion contraction upwind schemes with Heun timestepping with uniform time step $\Delta t = 0.1h$.

with $\varphi(x, y) := \cos(\pi\sqrt{x^2 + (y - 0.25)^2})^4$. The "hump" is Lie advected on the diagonal of the domain with velocity field $\mathbf{u} = (2, 2)^\top$. The forcing term in this experiment is set to zero, $\mathbf{f} = (0, 0)^\top$.

We compute the numerical errors associated with the spatial discretization, at final time $T = 0.5$. Figure 4.4 shows that first order convergence is attained both in the L^2-norm and in the H(div, Ω)-seminorm.

Piecewise linear approximation and interpolation
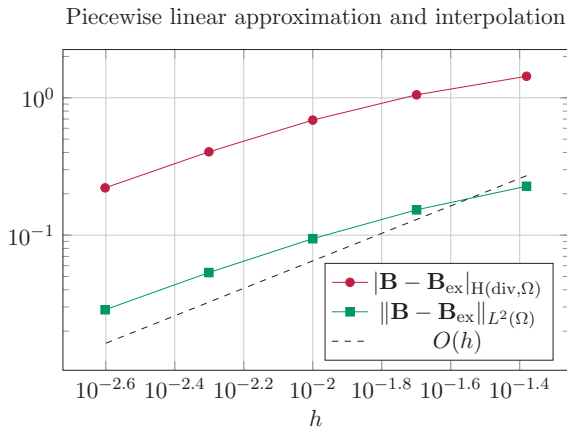
FIGURE 4.4. Advection of 1-forms. Non-solenoidal magnetic induction. Numerical convergence study of the piecewise linear extrusion contraction scheme. Heun timestepping and uniform time step $\Delta t = 0.1h$.

4.2. **Numerical Experiments for Extended Euler**

To experimentally gauge the performances of lowest order finite volume schemes for the extended Euler system derived in Section 3, we propose a two-dimensional MHD test with given magnetic induction field [6, Section 6]. More in details, the solution is smooth and known analytically at any point in space and time in the domain $\Omega \times I = [-5, 5]^2 \times [0, 0.5]$, see Section 4.3.1 for further details. Let $r(x, y, t) := \sqrt{(x - t)^2 + (y - t)^2}$, the flow is characterized by the following set of data,

$$\rho(x, y, t) = 1, \quad p(x, y, t) = 1 + \frac{1}{8\pi}(\mu^2(1 - r^2) - \kappa^2)e^{1-r^2},$$

$$\mathbf{u}(x, y, t) = (1, 1)^{\top} + \frac{\kappa}{2\pi} e^{1/2(1-r^2)}(t - y, x - t)^{\top}.$$

The ratio of specific heats is $\gamma = 5/3$ and the parameters $\kappa = \mu = 1$. The magnetic induction field $\mathbf{B}$ is given at each time step in analytic form as $\mathbf{B}(x, y, t) = \frac{\mu}{2\pi} e^{1/2(1-r^2)}(t - y, x - t)^{\top}$. We aim at assessing the convergence properties of the scheme. Explicit Euler timestepping ($C_{\mathsf{CFL}} = 0.4$) is coupled with a piecewise constant finite volume discretization in space and tested with different approximate Riemann solvers. In Figure 4.5, the L^1-error of the primitive variables at final time $T = 0.5$ is reported. As expected, first order convergence is observed.
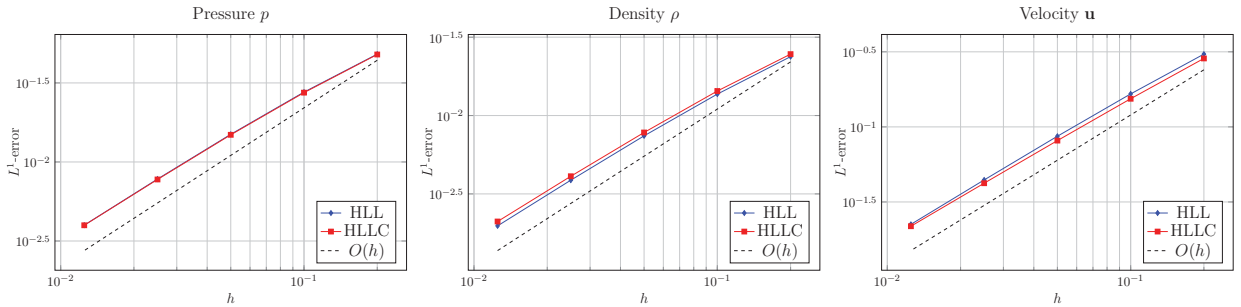
FIGURE 4.5. Smooth vortex. Accuracy test for finite volume discretizations of the extended Euler system with given analytic $\mathbf{B}$ field. Different approximate Riemann solvers are considered. In the legend, HLL refers to the two-wave Riemann solver with wave speeds as in (3.6) and HLLC to the three-wave Linde solver.

4.3. **Numerical Experiments for Ideal MHD**

In this section we numerically study the fully coupled FV-FEEC scheme described in Section 3.2 on a set of two-dimensional ideal MHD benchmark simulations. In particular, for the magnetic advection subproblem we focus on the potential-based formulation (1.2), for which extrusion contraction upwind schemes have been tested in Section 4.1.1.

Remark 4.1 (Collisional fluid velocities)**.** On a tensor product partition $\mathcal{T}_h$ of the computational domain Ω, the fluid velocity resulting from lowest order finite volume discretizations of the extended Euler equations is a $\mathcal{T}_h$-piecewise constant function $\mathbf{u} \in \mathcal{P}_0(\mathcal{T}_h)$ (collecting the cell averages of the fluid velocity in each mesh element). However, the extrusion contraction upwind discretization of the advection problem entails an upwind interpolation of the Lie derivative which requires the knowledge of the velocity field at the mesh nodes and along edges. One can approximate the value at a given node by averaging the values from the elements sharing the node. This pointwise interpolation might appear rather crude. It is especially the case in the presence of colliding or diverging velocity at a node or an edge where one might lose information on the local dynamics.

In MHD, the fast magnetosonic wave speed provides a good indicator of the flow dynamics. Hence, in the FV-FEEC algorithm implemented in the numerical experiments below, the upwind direction entering the discrete Lie derivative at the mesh cells where the velocity field is colliding or diverging is determined by the fast MHD wave speed, namely $c_f^M := (c_f^{M,1}, c_f^{M,2})$, where $c_f^{M,\ell}$, $\ell \in \{1, 2\}$ is defined as in (3.5). Once the upwind direction has been uniquely identified at each mesh cell, the pointwise advection velocity at the nodes is taken from within the upwind element.

4.3.1. *Accuracy Test: Smooth Vortex*

In order to experimentally assess the accuracy of the lowest order FV-FEEC scheme, we present a genuinely two-dimensional (non-trivial) MHD test where the solution is known analytically at every point in space and time. The smooth vortex test was proposed in [6, Section 6] (a scaling factor $\sqrt{4\pi}$ has been absorbed in the definition of $\mathbf{B}$). The problem is associated with a smoothly varying fluid vortex which propagates at a $\pi/4$ angle to the computational mesh on the domain $\Omega = [-5,5]^2$ with periodic boundaries. The initial condition is given by a vortex characterized by fluctuations of the velocity and of the magnetic field, superimposed to an unperturbed MHD flow $\mathbf{U}_0 = (\rho_0, p_0, u_0^1, u_0^2) = (1,1,1,1)$, $\mathbf{B}_0 = \mathbf{0}$. Let $r(x,y,t) := \sqrt{(x-t)^2 + (y-t)^2}$, the flow is described by the following set of data,

$$\rho(x,y,t) = 1, \quad p(x,y,t) = 1 + \frac{1}{8\pi}(\mu^2(1-r^2) - \kappa^2)e^{1-r^2},$$

$$\mathbf{u}(x,y,t) = \mathbf{u}_0 + \frac{\kappa}{2\pi}e^{1/2(1-r^2)}(t-y, x-t)^\top,$$

$$\mathbf{B}(x,y,t) = \frac{\mu}{2\pi}e^{1/2(1-r^2)}(t-y, x-t)^\top, \quad A(x,y,t) = \frac{\mu}{2\pi}e^{1/2(1-r^2)}.$$

As initial datum we take $\mathbf{U}(\mathbf{x},0)$ with $\mathbf{u}_0 = (u_0^1, u_0^2)^\top = (1,1)^\top$, $\kappa = \mu = 1$ and $A(\mathbf{x},0)$ for the magnetic advection subproblem. The ratio of specific heats is $\gamma = 5/3$. The time interval is $I = [0, 0.5]$. Explicit Euler is used as timestepping with CFL constant $C_{\mathsf{CFL}} = 0.4$.

The numerical convergence study on smooth solutions in Figure 4.6 (left) displays first order convergence of the errors of the scalar magnetic potential in the norms associated with the Bochner spaces $L^\infty(I, L^2(\Omega))$ and $L^\infty(I, H^1(\Omega))$ and defined as $\|A\|_{L^\infty(I,H)} := \text{ess sup}_{t \in I} \|A(t)\|_H$ on the Sobolev space $(H, \|\cdot\|_H)$. Analogous conclusions can be drawn from Figure 4.6 (right) where the $L^\infty(I, L^1(\Omega))$-errors of the $\mathcal{T}_h$-piecewise constant MHD primitive variables are illustrated.

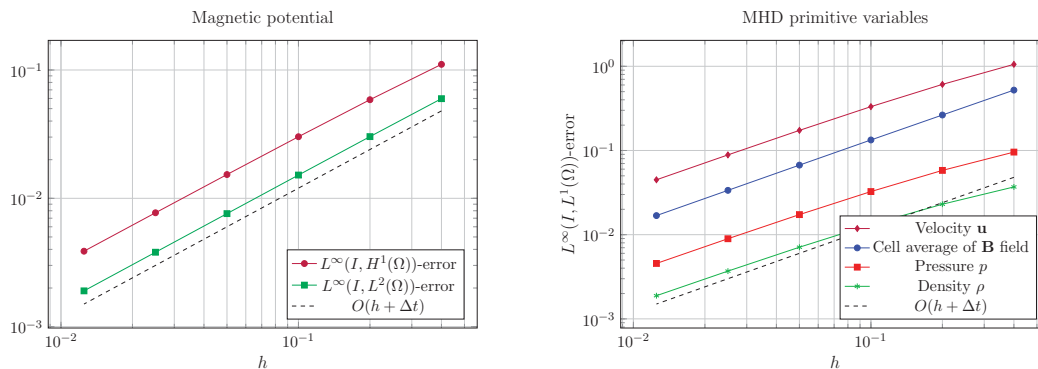FIGURE 4.6. Accuracy test for full ideal MHD system. $L^\infty(I, L^2(\Omega))$- and $L^\infty(I, H^1(\Omega))$-error of the magnetic potential (left), $L^\infty(I, L^1(\Omega))$-error of the MHD primitive variables (right). Piecewise constant finite volume discretizations of the extended Euler system with HLL Riemann solver and piecewise linear extrusion contraction scheme for the advection of the magnetic potential, explicit Euler timestepping and $C_{\mathsf{CFL}} = 0.4$.

4.3.2. *Super-Fast Expansion: Shock Tube Test*

To the aim of testing the robustness of numerical schemes in delivering physically admissible solutions of the one-dimensional MHD equations, a super-fast expansion simulation has been used in e.g. [30,

Section 6.1 p. 338] and [14, Section 3.2]. With the same goal, we study a variant of the foregoing test case in a formally two-dimensional setting. Let us consider the domain $\Omega = [0,1]^2$ with periodic upper $\{\mathbf{x} \in \Omega : y = 1\}$ and lower $\{\mathbf{x} \in \Omega : y = 0\}$ boundaries. In the remaining part of $\partial\Omega$, non-reflecting Neumann type boundary conditions are applied to the conserved variables of the extended Euler system, and outflow boundary conditions to the advection problem since the evolution of the velocity field does not induce any inflow boundary on the considered time interval $I = [0, 0.2]$. We perform planar two-dimensional simulations of the one-dimensional (in the x-direction) shock tube test with initial data

$$\rho_0(x, y) = 1, \quad p_0(x, y) = 0.45,$$

$$u_0^1(x, y) = \begin{cases} -3.1 & \text{if } x < 0.5, \\ 3.1 & \text{if } x > 0.5, \end{cases} \qquad u_0^2(x, y) = 0,$$

$$\mathbf{B}_0(x, y) = (0, 0.5)^\top, \quad A_0(x, y) = -0.5x,$$

and $\gamma = 5/3$ as ratio of specific heats. As the problem involves a left-moving and a right-moving rarefaction wave, the central region is subject to a super-fast expansion yielding very low density and pressure. In [14, Section 3.2], it has been observed that linearized Roe solvers for finite volume discretizations of the full MHD system usually run into negative pressure and density in such test case. The FV-FEEC scheme proves positively conservative at all tested resolutions, see Figure 4.7.
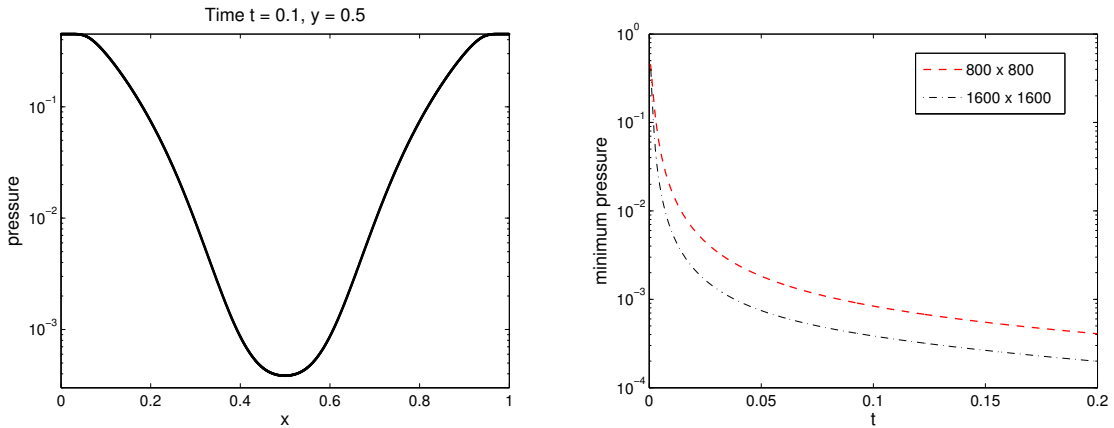

FIGURE 4.7. Super-fast expansion. Semi-logarithmic plot of the projection onto $\{\mathbf{x} \in \Omega : y = 0.5\}$ of the numerical pressure (left) at the intermediate time $t = 0.1$. Numerical discretization on a 1600×1600 Cartesian mesh with Heun timestepping and $C_{\mathsf{CFL}} = 0.4$. Lowest order extrusion contraction for the advection of the magnetic potential and finite volume scheme for the extended Euler equations using the HLL approximate Riemann solver. On the right, semi-logarithmic evolution plot of the minimum of the discrete pressure until time $t = 0.2$ at 800×800 and 1600×1600 mesh resolutions.

4.3.3. *Orszag–Tang Benchmark*

The so-called Orszag–Tang vortex system was introduced in [32, Section 3], and describes the transition to supersonic turbulence in the MHD equations. The development of shock waves and the complex interaction between various shocks with different speed, which characterized the solution, makes the Orszag–Tang benchmark a challenging test for numerical methods. Let us consider the domain $\Omega =$

247

$[0,2]^2$ with periodic boundary conditions. The time interval is $I = [0,1]$. The initial conditions for the primitive fluid variables, the magnetic induction field $\mathbf{B}$ and the magnetic potential A are

$$\rho_0(x,y) = \gamma^2, \quad p_0(x,y) = \gamma, \quad \mathbf{u}_0(x,y) = (-\sin(\pi y), \sin(\pi x))^\top,$$

$$\mathbf{B}_0(x,y) = (-\sin(\pi y), \sin(2\pi x))^\top, \quad A_0(x,y) = \frac{1}{\pi}\cos(\pi y) + \frac{1}{2\pi}\cos(2\pi x),$$

and $\gamma = 5/3$ is the gas constant. Since the Orszag–Tang test is a widely used benchmark, we can compare the performances of the FV-FEEC scheme with the numerical discretizations of [14]. As reported in [14, Section 3.3], finite volume schemes for the full MHD system based on Roe solvers, two-wave HLL and three-wave HLLC solvers, with and without divergence cleaning (via projection methods), experienced negative pressures at fine mesh resolution.

In Table 4.1, we compare the maximum pressure at final time $T = 1$ of the lowest order FV-FEEC discretization with the results reported in [14, Table 2.2] for the first order finite volume schemes HLL/SUS and HLLC/SUS from [14] and [12]. The reported values are comparable at all mesh resolutions: the HLLC solver for FV-FEEC gives slightly more "accurate" results, as experienced in Section 4.2 when testing approximate Riemann solvers on the extended Euler system, and shown in Figure 4.8 in comparison with a second order accurate "reference" solution[2].

$\sharp\mathcal{T}_h$	HLL/SUS [14, Table 2.2]	FV-FEEC HLL	HLLC/SUS [14, Table 2.2]	FV-FEEC HLLC
100×100	4.94	4.38	5.04	5.05
200×200	5.39	5.29	5.41	5.65
400×400	5.79	5.84	5.81	5.91
800×800	6.05	6.06	6.07	6.10
1600×1600	6.21	6.20	6.22	6.23

TABLE 4.1. Orszag–Tang benchmark. Maximum value of the discrete pressure at final time obtained with the FV-FEEC scheme with two-wave HLL and three-wave HLLC Riemann solvers, and compared with the values from the finite volume discretizations HLL(C)/SUS of [14].

Finite volume schemes are, by construction, conservative methods. However, the conservation property is not naturally inherited by the coupled FV-FEEC discretizations. In order to numerically assess the conservation properties of the FV-FEEC scheme, we monitor the evolution of the mean, on the computational domain Ω, of the conserved variables over time. Given the scalar function $f(\mathbf{x}, t)$ and the initial datum $f_0(\mathbf{x})$, we compute, on the partition of the temporal interval, the following error,

$$\mathcal{E}(f) := \max_{1 \leq m \leq N} |\overline{f}^m - \overline{f}_0|, \qquad \overline{f}^m := \fint_\Omega f(\mathbf{x}, t^m) d\mathbf{x} \quad \text{and} \quad \overline{f}_0 := \fint_\Omega f_0(\mathbf{x}) d\mathbf{x}. \tag{4.3}$$

Whenever needed we consider the relative error $\mathcal{E}_r(f) := \mathcal{E}(f)/|\overline{f}_0|$. Table 4.2 reports the values of the aforementioned error on the conserved MHD variables and for different mesh refinements: perfect conservation.

In Figure 4.9, we report the L^1-error of the primitive MHD variables at final time $T = 1$ computed with respect to the second order "reference" solution. The observed convergence rate is around 0.6.

Finally, the ability of the FV-FEEC scheme to reproduce physically reliable solutions with rather sharp resolution of the shock fronts is gauged in Figures 4.10 and 4.11, see also the results available in literature e.g. [13, Section 3.4] or [40, Section 6.4]. The lowest order FV-FEEC is admittedly diffusive

---

[2]The "reference" solutions used throughout the present section were provided by R. Käppeli, SAM, ETH Zürich, and based on the FISH code [27].
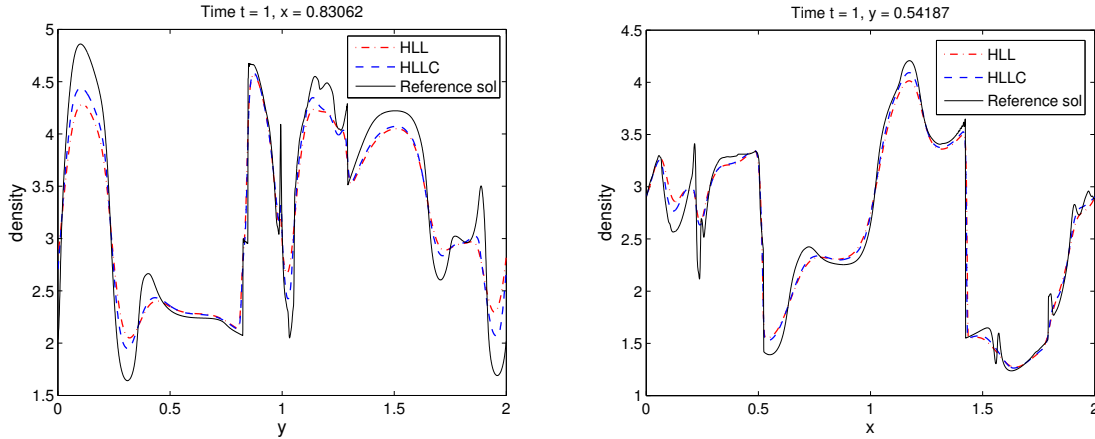
FIGURE 4.8. Orszag–Tang benchmark. Projections of the discrete density for constant values of the x-coordinate (left) and y-coordinate (right). Numerical discretization on a 1600×1600 Cartesian mesh. The finite volume scheme for the extended Euler equations is based on two-wave HLL and three-wave HLLC approximate Riemann solver. Heun timestepping with $C_{\mathsf{CFL}} = 0.4$. A second order accurate finite volume solution on 3200×3200 mesh elements is used as "reference" solution.

$\sharp \mathcal{T}_h$	$\mathcal{E}_r(\rho)$	$\mathcal{E}(\rho u^1)$	$\mathcal{E}(\rho u^2)$	$\mathcal{E}(B_1)$	$\mathcal{E}(B_2)$	$\mathcal{E}_r(E)$
200×200	1.3097e−15	2.1723e−11	4.0363e−12	1.8402e−11	4.5034e−12	2.1552e−15
400×400	1.8335e−15	1.3512e−10	3.3280e−11	2.0040e−10	3.4728e−10	1.8236e−15
800×800	2.2264e−15	4.1668e−10	1.0388e−10	9.8822e−10	7.6756e−10	2.8183e−15
1600×1600	3.6671e−15	5.6204e−09	5.9614e−10	2.0064e−09	4.8494e−09	3.1498e−15

TABLE 4.2. Orszag–Tang benchmark. Conservation properties of the FV-FEEC scheme. "Error" (4.3) of the MHD conserved variables at different mesh resolutions.
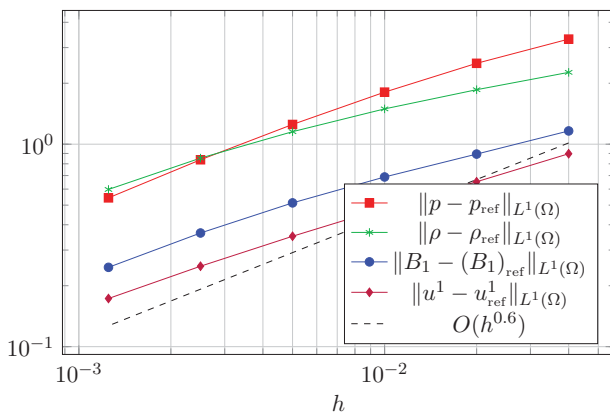

FIGURE 4.9. Orszag–Tang benchmark. Plot of the L^1-error vs. the mesh width h. The error of the MHD primitive variables is computed at final time $t = 1$ and with respect to a "reference" solution on a 3200×3200 mesh.

and does not capture all the complex shock interaction features visible in the second order accurate solution in Figure 4.11 (right column). Neither the FV-FEEC nor the second order "reference" solution

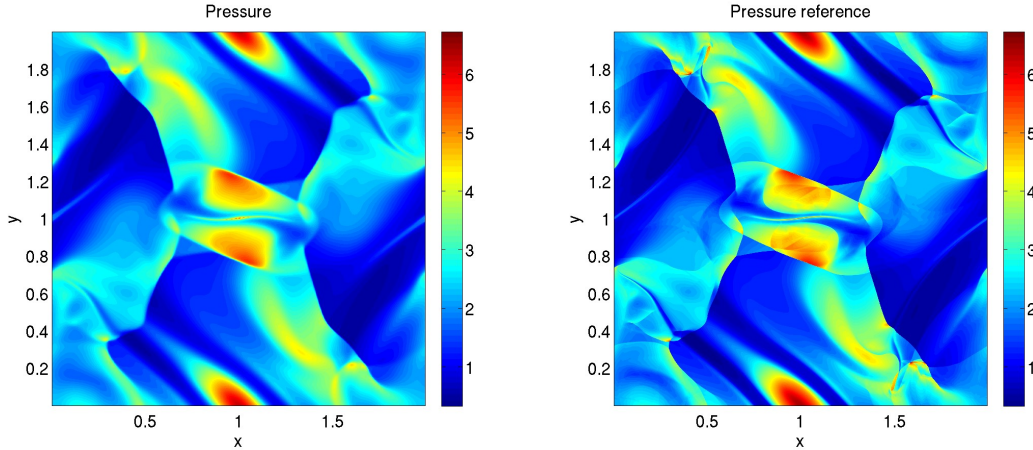manage to reproduce the current sheet in the second component of the **B** field at the center of the domain.

FIGURE 4.10. Orszag–Tang benchmark. Pressure. On the left, numerical solution on a 1600×1600 Cartesian mesh obtained with the FV-FEEC scheme and Heun timestepping with $C_{\mathsf{CFL}} = 0.4$. Finite volume scheme for the extended Euler equations based on the HLL approximate Riemann solver. The color map is scaled to the extrema of the "reference" solution on a 3200×3200 mesh (right column).

4.3.4. *Rotor Problem*

A key dimensionless parameter for ideal MHD models is the so-called *plasma beta*, the ratio of thermal to magnetic pressure, $\beta = 2\mu_0 p / \|\mathbf{B}\|_{L^2}^2$, where μ_0 is the permeability of free space. Delivering physically admissible solutions in presence of low-beta plasmas ($\beta \ll 1$) is particularly challenging for numerical schemes. The rotor problem provides a numerical test for the low-beta plasma setting. It was introduced in [7, Section 3.1] to test the emergence and propagation of torsional Alfvén waves. The interior of the rotor is characterized by low values of the pressure, so that the test is also well-suited to attest the robustness of a numerical method in preserving positivity. The initial set up consists of a dense spinning cylinder (the rotor) of radius 0.05, surrounded by the ambient fluid at rest which occupies the remaining part of the computational domain $\Omega = [0,1]^2$. The initial magnetic field is uniform but, as the rotor spins with the initial rotating velocity, the magnetic field in the x-direction starts wrapping around the rotor causing torsional Alfvén waves to propagate into the ambient fluid. As a result, the angular momentum will eventually decrease while the rotor will experience compression under the effect of the increased magnetic pressure assuming an oblong shape.

The physical problem is set up on an unbounded domain. This translates into artificial non-reflecting Neumann-type boundary conditions for the conserved variables entering the extended Euler system. Concerning the magnetic advection problem, the evolution of the velocity field guarantees that no inflow boundaries will occur at any time. The initial data are as explained above and characterized by,

$$\rho_0(x,y) = \begin{cases} 10 & \text{if } r < 0.1, \\ 1 + 9f & \text{if } 0.1 < r < 0.115, \\ 1 & \text{if } r > 0.115, \end{cases}$$
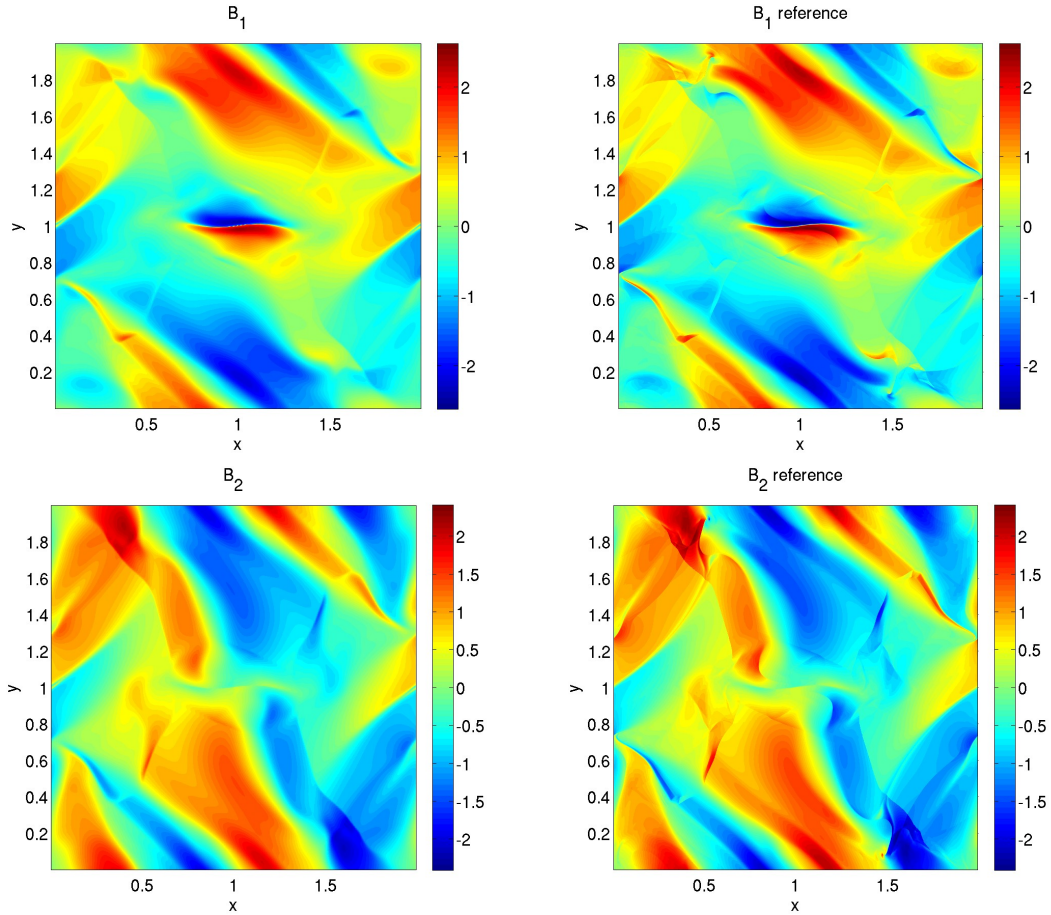
$$p_0(x,y) = 0.5,$$

Figure 4.11. Orszag–Tang benchmark. Magnetic induction field. On the left, numerical solution on a 1600×1600 Cartesian mesh obtained with the FV-FEEC scheme and Heun timestepping with $C_{\text{CFL}} = 0.4$. Finite volume scheme for the extended Euler equations based on the HLL approximate Riemann solver. The color map is scaled to the extrema of the "reference" solution on a 3200×3200 mesh (right column).

$$u_0^1(x,y) = \begin{cases} 5 - 10y & \text{if } r < 0.1, \\ (5 - 10y)f & \text{if } 0.1 < r < 0.115, \\ 0 & \text{if } r > 0.115, \end{cases} \quad u_0^2(x,y) = \begin{cases} 10x - 5 & \text{if } r < 0.1, \\ (10x - 5)f & \text{if } 0.1 < r < 0.115, \\ 0 & \text{if } r > 0.115, \end{cases}$$

$$\mathbf{B}_0(x,y) = \left(\frac{2.5}{\sqrt{4\pi}}, 0\right)^\top, \quad A_0(x,y) = \frac{2.5}{\sqrt{4\pi}}y,$$

where $r := \sqrt{(x - 0.5)^2 + (y - 0.5)^2}$, $f := (23 - 200r)/3$ and the gas constant is $\gamma = 5/3$. The simulation runs until time $T = 0.295$.

In order to numerically analyze the conservative properties of the FV-FEEC scheme tested on the rotor problem, Table 4.3 reports the error (4.3) on the conserved variables.

The FV-FEEC performs robustly also in the rotor test, as attested by Figure 4.12. The scheme captures many of the features of the MHD rotor flow being however rather diffusive when compared with the second order "reference" solution.

$\sharp\mathcal{T}_h$	$\mathcal{E}_r(\rho)$	$\mathcal{E}(\rho u^1)$	$\mathcal{E}(\rho u^2)$	$\mathcal{E}_r(B_1)$	$\mathcal{E}(B_2)$	$\mathcal{E}_r(E)$
200×200	4.3462e−04	4.1243e−11	2.3873e−12	4.8734e−04	3.0872e−04	9.3236e−04
400×400	8.2870e−05	9.7000e−12	4.3911e−11	9.9092e−05	6.5086e−08	1.7748e−04
800×800	5.5013e−06	3.5593e−11	4.5438e−10	6.7642e−06	1.1632e−10	1.1712e−05
1600×1600	1.0410e−07	1.6785e−08	5.7213e−07	1.3463e−07	1.7050e−09	2.2139e−07

TABLE 4.3. Rotor problem. Conservation properties of the FV-FEEC scheme. "Error" (4.3) of the MHD conserved variables at different mesh resolutions.
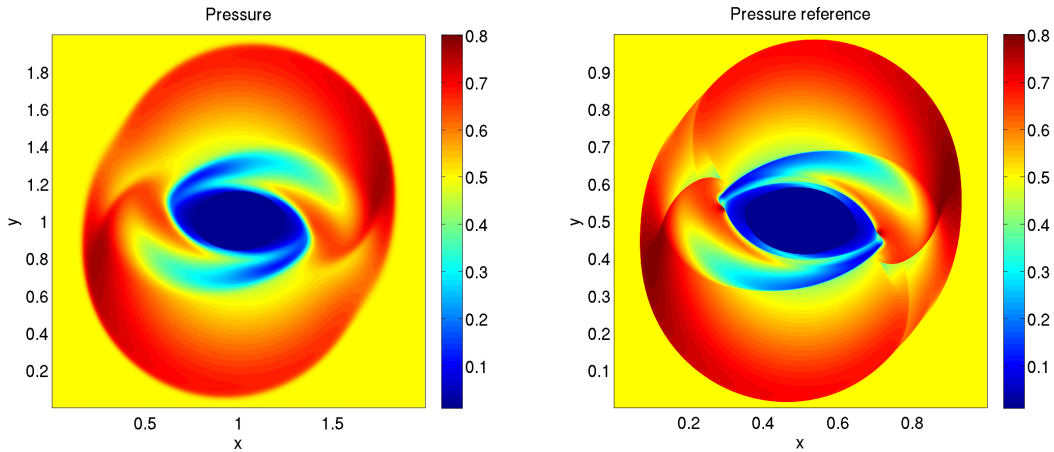

FIGURE 4.12. Rotor problem. Numerical solution on a 1600×1600 Cartesian mesh obtained with the lowest order FV-FEEC scheme and Heun timestepping with $C_{\mathsf{CFL}} = 0.4$. Finite volume scheme for the extended Euler equations based on the HLL approximate Riemann solver. The color map of the pressure plot is scaled to the extrema of the "reference" solution on a 3200×3200 mesh, shown on the top right plot.

4.3.5. *Blast Wave Problem*

As a last test case, we consider the isothermal blast wave problem proposed in [5, Section 6.2.2]. Note that we did not develop a numerical scheme tailored to the isothermal MHD model, we rather "emulated" the isothermal behavior by setting the ratio of specific heats close to unitary ($\gamma = 1.001$ in the forthcoming simulations). The blast wave benchmark is numerically challenging because it is characterized by a highly anisotropic explosion spreading out from a high density cloud initialized in a circular region of the domain. As pointed out in [5], failing to provide a control of the divergence of the induction field can engender detrimental small-scale fluctuations.

In the domain $\Omega = [0, 1]^2$ the initial data are,

$$\rho_0(x, y) = p_0(x, y) = \begin{cases} 100 & \text{if } \sqrt{(x - 0.5)^2 + (y - 0.5)^2} < 0.05, \\ 1 & \text{otherwise,} \end{cases}$$

$$\mathbf{u}_0(x, y) = \mathbf{0},$$

$$\mathbf{B}_0(x, y) = \left(\frac{5}{\sqrt{\pi}}, 0\right)^\top, \quad A_0(x, y) = \frac{5}{\sqrt{\pi}} y.$$

The simulation spans the time interval $I = [0, 0.09]$. Boundary conditions are of non-reflecting Neumann-type for the extended Euler variables, and the velocity field gives no inflow boundary.

The conservative properties of the scheme are numerically gauged in Table 4.4 where the error defined in (4.3) on the conserved variables is reported.

$\sharp\mathcal{T}_h$	$\mathcal{E}_r(\rho)$	$\mathcal{E}(\rho u^1)$	$\mathcal{E}(\rho u^2)$	$\mathcal{E}_r(B_1)$	$\mathcal{E}(B_2)$	$\mathcal{E}_r(E)$
200×200	8.5943e−14	1.3769e−12	5.8536e−11	7.8382e−15	4.3338e−11	8.9687e−14
400×400	2.6538e−15	8.6998e−12	7.5751e−10	1.7876e−15	1.7969e−10	3.9629e−15
800×800	2.0471e−15	1.8790e−11	1.4140e−09	2.8231e−15	1.1313e−10	9.6211e−15
1600×1600	2.1693e−14	7.6349e−08	6.4150e−07	9.9568e−14	5.3582e−09	1.8401e−14

TABLE 4.4. Blast wave test. Conservation properties of the FV-FEEC scheme. "Error" (4.3) of the MHD conserved variables at different mesh resolutions.

Numerical instabilities are a typical outcome of the blast wave test even for lowest order finite volume approximations of the full MHD system, see [13, pp. 356-357]. The blast wave MHD flow is characterized by outward- and inward-going fast magnetosonic shock and the magnetic induction field experiences a strong compression on account of the explosion. As it can be observed in Figure 4.13, the FV-FEEC scheme is robust, oscillations-free and it approximates the shocks rather sharply. The second row of Figure 4.13 shows the magnetic induction field lines: no fluctuations are observed, not even in the middle of the computational domain (compare with [5, Figure 9] and [13, Figure 8]).

5. **Concluding Remarks**

We have developed a family of numerical methods to solve the single-fluid standard MHD problem by coupling two different spatial discretizations of fluid and electromagnetic variables. The evolution of the electromagnetic fields relies on FEEC-based extrusion contraction upwind schemes. These methods are characterized by an intrinsic upwinding, which acts as a linear stabilization in the presence of boundary and internal layers, and by the fact that the resulting discrete Lie derivative commutes with the exterior derivative. This implies that in MHD the divergence constraint is satisfied exactly, and no mesh-staggering of fluid and electromagnetic variables, typical of constrained transport and "central schemes" for hyperbolic problems, is required. Although supported by numerical evidence, a rigorous stability and convergence analysis of the extrusion contraction upwind schemes is still an open problem.

Concerning the fluid dynamics part of the MHD model, we designed finite volume schemes hinged on approximate Riemann solvers tailored to accommodate the presence of the magnetic induction, which enters the system of conservation laws as a varying coefficient. The further adaptation of this construction to design numerical fluxes yielding a discrete version of the entropy inequality would pave the way to entropy stable schemes of arbitrarily high order.

The lowest order fully coupled FV-FEEC schemes are first order accurate for smooth solutions, possess built-in structure preserving properties, and perform robustly in many challenging MHD benchmark tests. The promising numerical results obtained when using discretizations of the electromagnetic fields based on discrete differential forms, even in the presence of complex flows, suggest that structure preserving conforming discretizations can be competitive also in computational fluid dynamics, typically preserve of finite volume and discontinuous Galerkin methods. Analogous splitting-based numerical methods for the MHD system obtained via fully discontinuous Galerkin discretizations of the potential-based advection problem (by staggering the magnetic potential with respect to the fluid variables similarly to a Yee-type scheme [41]) yield unphysical solutions on some challenging benchmark tests, as documented in [33, Section 7.2].
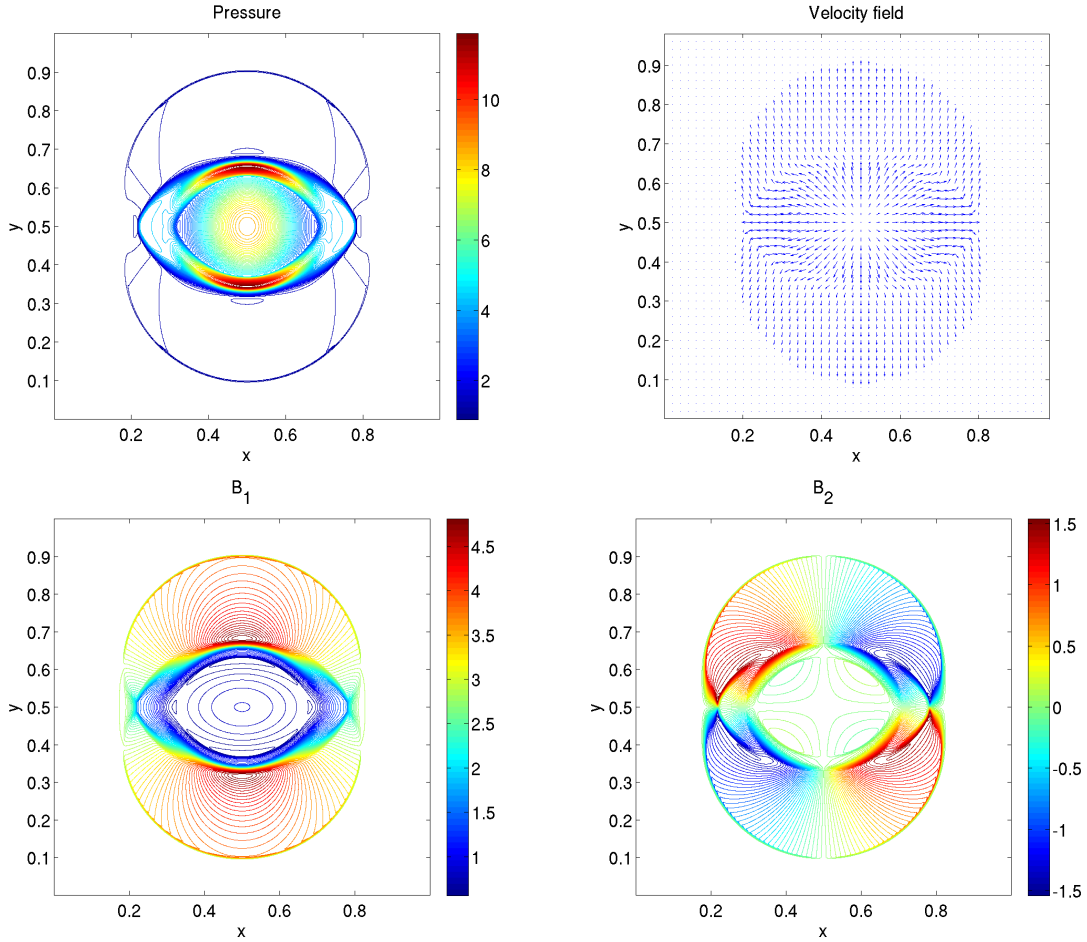
FIGURE 4.13. Blast wave test. Numerical discretization on a 1600×1600 Cartesian mesh with lowest order FV-FEEC scheme and Heun timestepping, $C_{\text{CFL}} = 0.4$. Finite volume scheme for the extended Euler equations using HLL approximate Riemann solver.

5.1. **Towards Higher Order FV-FEEC Schemes**

The promising numerical results obtained with the lowest order FV-FEEC discretizations can be a starting point for the design of second and higher order accurate schemes. The "synchronization" of the coupling step in Algorithm 1 ensures that no additional error associated with the splitting is introduced. We can therefore identify two main objectives for the derivation of formally high order FV-FEEC schemes:

(1) A high order discretization of the transient advection problem, able to supply a magnetic induction field accurate to the same order and endowed with a nonlinear mechanism for damping oscillations, capable of ensuring some TVD-like property without affecting the accuracy of the scheme;

(2) A high order extension of the FV schemes for the extended Euler equations via reconstruction and limiting, with controls on the preservation and evolution of physically admissible states.

Concerning the first aspect, when resorting to the potential-based formulation of the advection problem, high order numerical schemes should ideally curb the emergence of spurious oscillations in both

254

the magnetic potential and the magnetic induction field. In the context of extrusion contraction upwind schemes, *entropy viscosity methods* [17, 18] seem particularly attractive for the aforementioned task since they are based on the addition of a degenerate nonlinear diffusion term, tuned locally by a numerical viscosity proportional to the local entropy production. Specifically, the commutativity of the exterior derivative and the discrete Lie derivative allows the construction of nonlinear residual-based viscosity schemes for the advection of the magnetic potential, based, however, on the (entropy) residual of the magnetic induction equation. Preliminary results in this direction can be found in [33, Section 4.4]. In the alternative situation occurring when directly discretizing the magnetic induction problem, one should rely on the addition of artificial magnetic diffusion, based again on the induction residual. The augmented discrete operator obtained from the Lie derivative plus the second order artificial diffusion will still satisfy a commuting diagram property. On the other hand, it is not straightforward to gauge the effectiveness of the artificial viscosity since the nonlinear second order stabilization will have no impact on the kernel of the exterior derivative.

High order finite volume schemes for the extended Euler equations can be designed via ENO and WENO reconstruction techniques [19, 37]. The resulting schemes prove numerically robust and provide non-oscillatory solutions [33, Section 6.3.2], but they are not provably positively conservative. Devising a positivity fix for the finite volume discretizations of the extended Euler system in order to guarantee admissible updated and evolved fluid variables seems a challenging task since the lowest order scheme itself is not provably positively conservative. These issues represent intriguing topics for further investigation.

Acknowledgements

References

[1] D. N. Arnold and G. Awanou. Finite element differential forms on cubical meshes. *Math. Comp.*, 83(288):1551–1570, 2014.

[2] D. N. Arnold, D. Boffi, and F. Bonizzoni. Finite element differential forms on curvilinear cubic meshes and their approximation properties. *Numer. Math.*, 129(1):1–20, 2015.

[3] D. N. Arnold, R. S. Falk, and R. Winther. Finite element exterior calculus, homological techniques, and applications. *Acta Numer.*, 15:1–155, 2006.

[4] D. N. Arnold, R. S. Falk, and R. Winther. Finite element exterior calculus: from Hodge theory to numerical stability. *Bull. Amer. Math. Soc. (N.S.)*, 47(2):281–354, 2010.

[5] D. S. Balsara. Total variation diminishing scheme for adiabatic and isothermal magnetohydrodynamics. *The Astrophysical Journal Supplement Series*, 116(1):133–153, 1998.

[6] D. S. Balsara. Second-order-accurate schemes for magnetohydrodynamics with divergence-free reconstruction. *The Astrophysical Journal Supplement Series*, 151(1):149–184, 2004.

[7] D. S. Balsara and D. S. Spicer. A staggered mesh algorithm using high order Godunov fluxes to ensure solenoidal magnetic fields in magnetohydrodynamic simulations. *J. Comput. Phys.*, 149(2):270–292, 1999.

[8] A. Bossavit. Extrusion, contraction: their discretization via Whitney forms. *COMPEL*, 22(3):470–480, 2003.

[9] M. Brio and C.-C. Wu. An upwind differencing scheme for the equations of ideal magnetohydrodynamics. *J. Comput. Phys.*, 75(2):400–422, 1988.

[10] P. G. Ciarlet. *The finite element method for elliptic problems.* North-Holland Publishing Co., Amsterdam-New York-Oxford, 1978.

[11] B. Einfeldt. On Godunov-type methods for gas dynamics. *SIAM J. Numer. Anal.*, 25(2):294–318, 1988.

[12] F. G. Fuchs, K. H. Karlsen, S. Mishra, and N. H. Risebro. Stable upwind schemes for the magnetic induction equation. *M2AN Math. Model. Numer. Anal.*, 43(5):825–852, 2009.

[13] F. G. Fuchs, A. D. McMurry, S. Mishra, N. H. Risebro, and K. Waagan. Approximate Riemann solvers and robust high-order finite volume schemes for multi-dimensional ideal MHD equations. *Commun. Comput. Phys.*, 9(2):324–362, 2011.

[14] Franz G. Fuchs, S. Mishra, and N. H. Risebro. Splitting based finite volume schemes for ideal MHD equations. *J. Comput. Phys.*, 228(3):641–660, 2009.

[15] H. Goedbloed and S. Poedts. *Principles of Magnetohydrodynamics*. Cambridge University Press, 2004.

[16] S. Gottlieb, C.-W. Shu, and E. Tadmor. Strong stability-preserving high-order time discretization methods. *SIAM Rev.*, 43(1):89–112, 2001.

[17] J.-L. Guermond and R. Pasquetti. Entropy-based nonlinear viscosity for Fourier approximations of conservation laws. *C. R. Math. Acad. Sci. Paris*, 346(13-14):801–806, 2008.

[18] J.-L. Guermond, R. Pasquetti, and B. Popov. Entropy viscosity method for nonlinear conservation laws. *J. Comput. Phys.*, 230(11):4248–4267, 2011.

[19] A. Harten, B. Engquist, S. Osher, and S. R. Chakravarthy. Uniformly high-order accurate essentially nonoscillatory schemes. III. *J. Comput. Phys.*, 71(2):231–303, 1987.

[20] A. Harten, P. D. Lax, and B. van Leer. On upstream differencing and Godunov-type schemes for hyperbolic conservation laws. *SIAM Rev.*, 25(1):35–61, 1983.

[21] H. Heumann and R. Hiptmair. Extrusion contraction upwind schemes for convection-diffusion problems. SAM Report 2008-30, Seminar for Applied Mathematics, ETH Zürich, 2008.

[22] H. Heumann and R. Hiptmair. Convergence of lowest order semi-Lagrangian schemes. *Found. Comput. Math.*, 13(2):187–220, 2013.

[23] H. Heumann, R. Hiptmair, and C. Pagliantini. Stabilized Galerkin for transient advection of differential forms. *Discrete Contin. Dyn. Syst. Ser. S*, 9(1):185–214, 2016.

[24] R. Hiptmair. Canonical construction of finite elements. *Math. Comp.*, 68(228):1325–1346, 1999.

[25] R. Hiptmair. Finite elements in computational electromagnetism. *Acta Numer.*, 11:237–339, 2002.

[26] K. Hu, Y. Ma, and J. Xu. Stable finite element methods preserving $\nabla \cdot \mathbf{B} = 0$ exactly for MHD models. *Numer. Math.*, 135(2):371–396, 2017.

[27] R. Käppeli, S. C. Whitehouse, S. Scheidegger, U.-L. Pen, and M. Liebendörfer. FISH: a three-dimensional parallel magnetohydrodynamics code for astrophysical applications. *The Astrophysical Journal Supplement Series*, 195(20):1–16, 2011.

[28] K. H. Karlsen, S. Mishra, and N. H. Risebro. Semi-Godunov schemes for multiphase flows in porous media. *Appl. Numer. Math.*, 59(9):2322–2336, 2009.

[29] T. J. Linde. *A three-dimensional adaptive multifluid MHD model of the heliosphere*. PhD thesis, University of Michigan, Ann Arbor, MI, 1998.

[30] T. Miyoshi and K. Kusano. A multi-state HLL approximate Riemann solver for ideal magnetohydrodynamics. *J. Comput. Phys.*, 208(1):315–344, 2005.

[31] P. Mullen, A. McKenzie, D. Pavlov, L. Durant, Y. Tong, E. Kanso, J. E. Marsden, and M. Desbrun. Discrete Lie advection of differential forms. *Found. Comput. Math.*, 11(2):131–149, 2011.

[32] S. A. Orszag and C.-M. Tang. Small-scale structure of two-dimensional magnetohydrodynamic turbulence. *J. Fluid Mech.*, 90(1):129–143, 1979.

[33] C. Pagliantini. *Computational Magnetohydrodynamics with Discrete Differential Forms*. PhD thesis, Dis. no 23781, ETH Zürich, 2016.

[34] P.-A. Raviart and J.-M. Thomas. A mixed finite element method for 2nd order elliptic problems. In *Mathematical aspects of finite element methods (Proc. Conf., Consiglio Naz. delle Ricerche (C.N.R.), Rome, 1975)*. Springer, Berlin, 1977.

[35] H.-G. Roos, M. Stynes, and L. Tobiska. *Robust numerical methods for singularly perturbed differential equations*. Springer-Verlag, Berlin, 2008.

[36] D. Schötzau. Mixed finite element methods for stationary incompressible magneto-hydrodynamics. *Numer. Math.*, 96(4):771–800, 2004.

[37] C.-W. Shu and S. Osher. Efficient implementation of essentially nonoscillatory shock-capturing schemes. II. *J. Comput. Phys.*, 83(1):32–78, 1989.

[38] M. Tabata. A finite element approximation corresponding to the upwind finite differencing. *Mem. Numer. Math.*, 4:47–63, 1977.

[39] E. F. Toro, M. Spruce, and W. Speares. Restoration of the contact surface in the HLL-Riemann solver. *Shock Waves*, 4(1):25–34, 1994.

[40] G. Tóth. The $\nabla \cdot B = 0$ constraint in shock-capturing magnetohydrodynamics codes. *J. Comput. Phys.*, 161(2):605–652, 2000.

[41] K. Yee. Numerical solution of initial boundary value problems involving Maxwell's equations in isotropic media. *IEEE Transactions on Antennas and Propagation*, 14(3):302–30, 1966.